

Stable Anode-Free All-Solid-State Lithium Battery through Tuned Metal Wetting on the Copper Current Collector

Yixian Wang, Yijie Liu,* Mai Nguyen, Jaeyoung Cho, Naman Katyal, Bairav S. Vishnugopi, Hongchang Hao, Ruyi Fang, Nan Wu, Pengcheng Liu, Partha P. Mukherjee, Jagjit Nanda, Graeme Henkelman, John Watt, and David Mitlin*

A stable anode-free all-solid-state battery (AF-ASSB) with sulfide-based solid-electrolyte (SE) (argyrodite $\text{Li}_6\text{PS}_5\text{Cl}$) is achieved by tuning wetting of lithium metal on “empty” copper current-collector. Lithiophilic $1\ \mu\text{m}$ Li_2Te is synthesized by exposing the collector to tellurium vapor, followed by in situ Li activation during the first charge. The Li_2Te significantly reduces the electro-deposition/electrodissolution overpotentials and improves Coulombic efficiency (CE). During continuous electrodeposition experiments using half-cells ($1\ \text{mA cm}^{-2}$), the accumulated thickness of electrodeposited Li on $\text{Li}_2\text{Te-Cu}$ is more than $70\ \mu\text{m}$, which is the thickness of the Li foil counter-electrode. Full AF-ASSB with NMC811 cathode delivers an initial CE of 83% at 0.2C, with a cycling CE above 99%. Cryogenic focused ion beam (Cryo-FIB) sectioning demonstrates uniform electrodeposited metal microstructure, with no signs of voids or dendrites at the collector-SE interface. Electrodeposition is uniform and complete, with Li_2Te remaining structurally stable and adherent. By contrast, an unmodified Cu current-collector promotes inhomogeneous Li electrodeposition/electrodissolution, electrochemically inactive “dead metal,” dendrites that extend into SE, and thick non-uniform solid electrolyte interphase (SEI) interspersed with pores. Density functional theory (DFT) and mesoscale calculations provide complementary insight regarding nucleation-growth behavior. Unlike conventional liquid-electrolyte metal batteries, the role of current collector/support lithiophilicity has not been explored for emerging AF-ASSBs.

The higher capacity of Li versus graphite ($3861\ \text{mAh g}^{-1}$ vs $372\ \text{mAh g}^{-1}$) combined with high voltage cathodes results in an over 50% increase in the specific energy versus conventional ion-insertion anodes. Employing solid-state electrolytes (SEs) is a path toward greater battery safety since most inorganic SEs are non-flammable or have much higher ignition temperatures than organic-based electrolytes.^[1–10] All-solid-state batteries (ASSBs) can achieve the sought-after high energies when employing cathodes such as $\text{LiNi}_{0.8}\text{Mn}_{0.1}\text{Co}_{0.1}\text{O}_2$ (NMC811) and $\text{LiNi}_{0.5}\text{Mn}_{1.5}\text{O}_4$.^[11–15] Having the SEs be as thin as practically possible maximizes the energy density of the cells by both reducing the total weight and achieving voltage window closer to the theoretical value due to reduced impedance.^[16] Likewise, a thin metal anode is sought-after since it reduces the cell weight as well as the risk associated with accidental ignition of the metal.

It is known that sulfide SEs display highly promising ionic conductivities with the possibility of reaching $400\ \text{Wh kg}^{-1}$ at the cell-level.^[17–24] State-of-the-art sulfide SEs are drawing interest including thio-

LISICON ($\text{Li}_{10}\text{GeP}_2\text{S}_{12}$),^[25,26] $\text{Li}_6\text{PS}_5\text{X}$ ($\text{X} = \text{Cl}, \text{Br}, \text{I}$),^[27–31] and binary $\text{Li}_2\text{S-P}_2\text{S}_5$.^[32] These sulfide electrolytes typically display a bulk room-temperature Li-ion conductivity above $10^{-3}\ \text{S cm}^{-1}$. However, ASSBs using these sulfide SEs still suffer from

1. Introduction

Lithium (Li) metal-based batteries employ a Li-metal anode coupled with a conventional high voltage ceramic cathode.

Y. Wang, Y. Liu, H. Hao, R. Fang, N. Wu, P. Liu, D. Mitlin
Materials Science and Engineering Program & Texas Materials
Institute (TMI)
The University of Texas at Austin
Austin, TX 78712-1591, USA
E-mail: yijieliu@utexas.edu; david.mitlin2@utexas.edu
M. Nguyen, J. Cho, N. Katyal, G. Henkelman
Department of Chemistry
The University of Texas at Austin
Austin, TX 78712, USA

B. S. Vishnugopi, P. P. Mukherjee
School of Mechanical Engineering
Purdue University
West Lafayette, IN 47907, USA

J. Nanda
Applied Energy Division
SLAC National Laboratory
Menlo Park, CA 94025, USA

J. Watt
Center for Integrated Nanotechnologies
Los Alamos National Laboratory
Los Alamos, NM 87545, USA

 The ORCID identification number(s) for the author(s) of this article can be found under <https://doi.org/10.1002/adma.202206762>.

DOI: 10.1002/adma.202206762

several major shortcomings.^[33–36] One key issue is the reactivity between the sulfides and both electrodes, which leads to an impedance rise associated with the formation of a mixed conducting interphase (MCI).^[23,37–46] The interface between the metal anode and the SE should be either thermodynamically stable or be passivated to be kinetically stable. Sulfide SEs are not thermodynamically stable at 0 V versus Li/Li⁺, forming either MCI or a (partially) kinetically stabilized solid electrolyte interphase (SEI). For example, thio-LISICON type electrolyte Li₁₀GeP₂S₁₂ has an excellent conductivity around 10^{−2} S cm^{−1} but displays an unstable MCI due to the reduction of Ge⁴⁺ to Ge²⁺ and Ge⁰ upon contact with Li metal.^[47–49] Binary Li₂S-P₂S₅ also displays such an instability.^[50,51]

Argyrodite SEs such as Li₆PS₅Cl (LPSCl) and Li₆PS₅Br (LPSBr) form terminal decomposition products such as Li₃P and Li₂S at the metal anode. However, it is the presence of halide-based decomposition products such as LiCl that kinetically stabilizes the interface.^[52–54] For example, substantially improved ASSB performance has been achieved with “sandwich” structures such as LPSCl/LGPS/LPSCl.^[11] The lithium halide phases formed at the interface may also be effective in reducing the extent of dendrite growth in such systems. Research efforts with argyrodites have focused on introducing thin film protective interlayers between the metal anode and the SE, or constructing hybrid cell architectures.^[55–58] In polymer-based Li-SSBs, interlayers based on Li–Pt alloys^[59] and LiI^[60] have been demonstrated to be highly effective. Without such interface modification strategies, both Li electrodeposition and electrodisolution processes display critical current density (for dendrites and/or voids) that is too low. Sizable voids will form above the critical current density, indicating that Li electrodisolution at the Li–SE interface is faster than Li diffusion and creep for replenishment. Researchers have also employed alloy anodes to reduce SE decomposition to suppress dendrite growth.^[61,62] While alloy anodes improve the cell’s interfacial stability, the cell voltage is subsequently decreased (e.g., Li–In ≈ 0.6 V vs Li/Li⁺, Li–Al ≈ 0.4 V, and Li–Si ≈ 0.3 V).^[63–66] The external stack pressure also plays a critical albeit complex role in determining the critical currents. The critical stack pressure for ASSBs is closely related to the current density, area capacity, and temperature. When area capacity and temperature are constant, a stack pressure in the 10 MPa range is required to prevent voids formation and hence enable battery cycling. For example, Bruce et al. estimated a pressure over 7 MPa is needed for Li cycling at 1 mA cm^{−2} or higher.^[67]

For most ASSB architectures, a relatively thick metallurgically rolled lithium is employed with the capacity of the metal anode far exceeding the capacity of the cathode.^[45,68] Limiting the amount of lithium is essential to achieving ASSBs with the targeted energy density.^[69–72] For example, anode-free Li batteries can deliver a 30% higher specific energy density than identical cells with three times excess Li.^[73,74] Scheme S1, Supporting Information, illustrates the key differences for a Li-ion ASSB (LI-ASSB) with graphite-based ion storing anode (left), an Li-metal ASSB (LM-ASSB) with conventional thick lithium metal anode (center), and anode-free ASSB (AF-ASSB) (right) with an “empty” current collector. The differences concern the cell architecture, the achievable specific energy, and the ion storage mechanisms. Working backwards from the estab-

lished energy values for an LI-ASSB, it may be observed that the AF-ASSB configuration offers significantly higher energy density. An AF-ASSB also should have lower cost and less critical supply constraints due to the absence of surplus Li metal or of ion storing materials such as graphite. However, electrodepositing/electrodisolving Li directly onto a blank current Cu collector (AF-ASSB) involves a series of challenges not encountered when a Li foil is employed as the support (LM-ASSB). These hurdles will be discussed in detail throughout this manuscript in the context of experimental and simulation results. Existing anode-free studies focus on liquid electrolyte-based batteries, with the concept receiving much less attention for ASSBs. Pioneering development of AF-ASSBs were first reported in thin-film solid-state batteries using Li phosphorus oxynitride (LiPON).^[75] The LiPON electrolyte is stable with Li and is straightforward to deposit using magnetron sputtering.^[76,77] However its low ionic conductivity (≈10^{−6} S cm^{−1}) precludes its use as the primary electrolyte for thicker/larger cells. In related work, Sakamoto et al. studied the feasibility of garnet solid electrolyte Li₇La₃Zr₂O₁₂ (LLZO) for AF-ASSBs.^[78]

Achieving stable cycling behavior in an AF-ASSB remains a challenge due to the ongoing loss of lithium that reacts with SE. To date, there have not been reports of anode-free sulfide-based ASSB configurations. In this study, we demonstrate that a difference in the solid-state wetting of lithium on an anode current collector is a key determinant for AF-ASSB stability. We employ a Li-activated tellurium coating (transformed to 1 μm Li₂Te) on standard planar copper current collector coupled with an argyrodite SE (LPSCl) to enable uniform lithium metal electrodeposition and electrodisolution, while the baseline uncoated foil is inhomogeneously wetted. This leads to tremendous differences in the electrochemical performance and associated microstructure of the AF-ASSB cells. The rationale for choosing Li₂Te was a combination of factors: We sought a kinetically and/or thermodynamically stable structure that was lithiophilic. It also should have been straightforward to fabricate and would be potentially scalable, for example not requiring advanced high vacuum deposition methods that are incompatible with practical battery manufacturing. Through a combination of electroanalysis and density functional theory (DFT) simulation, we converged on the electrochemically irreversible (at test conditions) reaction of 2Li⁺ + 2e[−] + Cu₂Te ⇒ Li₂Te + 2Cu, the dense interspersions of the two terminal phases being both lithiophilic and electrically conductive. The initial tellurization process of a standard copper foil surface could be accurately performed using a standard low-temperature furnace with a molten Te crucible in an argon atmosphere. The electrochemical stability of the Li₂Te is a critical aspect of the design approach and makes this methodology distinct from the reversible alloying approaches previously employed to guide electrodeposition in ASSBs. Employing reversible alloy anodes such as Li–Mg, Li–Sn, Li–In, and Na–Sn alloys, and passivating the metal anode surface with electronically insulating layers have been shown to be effective with conventional ASSBs where there is a relatively thick metal anode that serves as an ion reservoir to make up for the CE losses.^[26,79–81] By contrast, the electrochemically stable Li₂Te + Cu approach eliminates the volumetric expansion–contraction associated with reversible alloying–de-alloying of elements such as Al, Mg, In, Ga, and Sn, as well as

intercalation–deintercalation volume changes associated with carbon-based supports.^[82–84] The repeated volume changes at the anode are known to promote SEI growth, something that would be unacceptable with anode-free architectures due to the cathode-limited supply of Li. Unlike the oxide and hydride passivation approaches, an electrically conductive interface to the current collector is maintained, aiding rate capability—power of the battery.

The role of metal wetting in dendrite growth has been studied for liquid-electrolyte-based metal batteries. With liquid-electrolyte metal batteries, support surface chemistry will affect the metal electrodeposition–electrodissolution kinetics and consequently dendrite growth.^[85–92] However, to our knowledge, such knowledge does not exist for emerging all-solid-state-batteries (ASSBs) or anode-free all solid-state-batteries (AF-ASSBs). In fact, within the energy storage community there is little agreement regarding commonalities and differences for liquid electrolytes versus ASSBs and AF-ASSBs. The latter two are based on fundamentally different architectures than liquid cells, with distinct issues related to mechanical compatibility of the non-flowing SE and the volume-changing anode/cathode.^[23,45,56,93] With ASSBs and AF-ASSBs, the role of metal wetting on the anode-free current collector is also distinct from the thick metal anode—SE compatibility affects detailed for garnet-based electrolytes.^[94–96] Therefore, elucidating the role of current collector lithiophilicity in the electrochemical stability of AF-ASSBs represents a new advance that should significantly influence next-generation materials and system design.

2. Results and Discussion

The tellurium-coated copper current collector (Te–Cu) was prepared using a one-step tellurization process. In summary, a section of cleaned battery-grade Cu foil was placed on top of a crucible containing a set amount of Te powder, which was transferred to a programmed furnace and annealed at 600 °C for 1 h under continuous Ar flow. During this process, the Cu surface reacts with the evaporated Te to form a uniform layer of copper telluride (Cu₂Te) intermetallic crystallites. The calculated mass loading of Cu₂Te is 0.4 mg cm⁻². Figure S1a, Supporting Information, shows X-ray diffraction (XRD) analysis of the as-synthesized coating. Baseline Cu foil belongs to the *Fm-3m* space group (*a* = 0.3613 nm) and exhibits three characteristic peaks at 43.3°, 50.4°, and 74.1°, corresponding to the 111, 200, and 220 reflections. After tellurization, four additional diffraction peaks at 12.1°, 24.4°, 27.2°, and 44.8° are present. These are associated with the 001, 100, 101, and 103 reflections of the Cu₂Te structure belonging to the *P6/mmm* space group (*a* = 0.4237 nm, *c* = 0.7274 nm). X-ray photoelectron spectroscopy (XPS) was performed to investigate the bonding of the layer. Figure S1b, Supporting Information, displays the high-resolution XPS spectrum of Te 3d. The Te²⁻ 3d_{5/2} (572.5 eV) and Te²⁻ 3d_{3/2} (582.9 eV) can be observed along with Cu LMM Auger. The high-resolution Cu 2p spectrum is shown in Figure S1c, Supporting Information, where peaks at 932.4 and 952.2 eV can be assigned to Cu⁰/Cu⁺ 2p_{3/2} and Cu⁰/Cu⁺ 2p_{1/2}, while the peaks at 934.2 and 954.0 eV are ascribed to Cu²⁺

2p_{3/2} and Cu²⁺ 2p_{1/2}. The XRD and XPS results confirm the formation of Cu₂Te on the copper surface after the tellurization process. The surface morphology of the Cu₂Te layer was characterized by scanning electron microscopy (SEM). As shown in Figure S1d,e, Supporting Information, the Cu₂Te crystallites uniformly grow on the Cu surface. Figure S1f–h, Supporting Information, shows the focused ion beam (FIB) cross-sectional SEM image along with the associated energy-dispersive X-ray spectroscopy (EDXS) elemental maps. The thickness of the Cu₂Te layer is about 1 μm, with the images further highlighting the geometrically uniform distribution of the crystallites on foil surface.

Electrochemical tests were carried out using poly(aryl-ether-ether-ketone) (PEEK) mold cells in a two-electrode configuration shown in Figure S2, Supporting Information. Tellurium-modified or (baseline) unmodified copper current collectors were employed as the working electrodes. Pure Li metal foil served as the reference and counter electrode. An argyrodite-type LPSCI SE was used as the separator, without any modifications or additional interlayers. To standardize the test, all cells were tested under a pressure of ≈13 MPa at room temperature. It should be pointed out that an external pressure of 13 MPa is well within the range reported in prior ASSB studies when employing either a Li foil reservoir or an ion anode such as silicon.^[12] In fact, the reported pressures needed for achieving sufficient interfacial contact while avoiding electrical shorting at open circuit are as high as 50–250,^[11] 40,^[97] and 50 MPa.^[12] In situ lithium activation of the Cu₂Te intermetallic was employed to fabricate the final Li₂Te coating layer directly on the collector. The electrochemical measurements were carried out in an asymmetric Li counter electrode–SE–current collector (Li|SE|CC) configuration in the PEEK cell. For the remaining of the discussion this configuration will be referred to as a “half-cell.” For AF-ASSBs, a configuration representative of current collector–SE–NMC811 (CC|SE|NMC) was employed. As will be demonstrated, the formation of Li₂Te is irreversible under the tested electrochemical conditions, meaning there is no Li source on the anode current collector.

Figure 1a shows the single galvanostatic discharge/charge profile of the Cu₂Te-coated foil employed for Li activation, tested at 0.1 mA cm⁻². The activation process entails a conversion reaction where Cu₂Te reacts with Li to form Li₂Te and Cu. The zoomed-in voltage–capacity curve is shown in Figure 1b. Two plateaus at ≈1.5 and 1.3 V can be observed, corresponding to the stepped lithiation of Cu₂Te.^[98] From the two figures it may be observed that to reverse this conversion reaction requires voltages substantially higher than the 1 V anodic limit used for the electrochemical experiments. According to Figure 1a, once the electrodeposited Li is electrodissolved there is negligible additional capacity. This important point is examined in more detail in Figure S3, Supporting Information. It may be observed that the Li₂Te-coated electrode delivered negligible capacity during the first delithiation process as well as in the sequent cycles, indicating that the conversion reaction is irreversible within an anodic voltage of 1 V. Therefore, the Li₂Te layer does not serve as a source of Li during subsequent testing. Lithium alloy anodes such as Mg, Al, Si, In, and Sn will reversibly de-alloy at relatively low anodic voltages (≈0.2 V for Mg,^[99,100] ≈0.4 V for Al,^[63,101] ≈0.3 V for Si,^[64,102] ≈0.6 V for In,^[103] and ≈0.2 V for

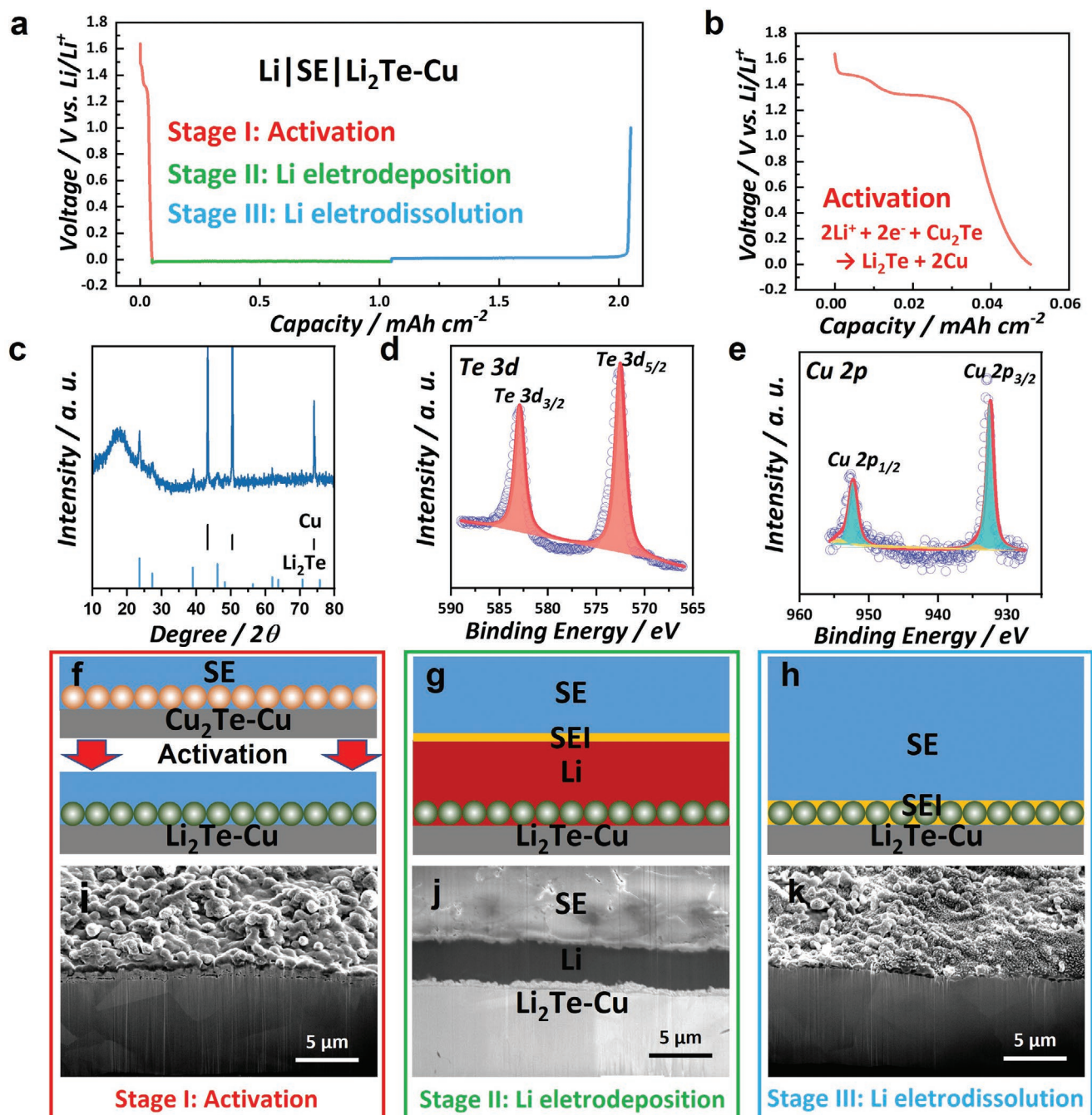


Figure 1. a) Galvanostatic discharge and charge profile of the Li|SE|Li₂Te–Cu cell at 0.1 mA cm^{−2} at cycle 1. b) Amplified discharge profile of the activation process. c) XRD pattern and d, e) XPS spectra of the Te–Cu electrode after activation. f–k) Schematic diagrams and top-down/cross-sectional SEM images of the Li|SE|Li₂Te–Cu cell after f, i) activation, g, j) electrodeposition 1 mA cm^{−2} Li, and h, k) electrodisolution to 1.0 V.

Sn^[104]). By contrast, Li₂Te requires an anodic voltage of 1.8 V to undergo a lithium-ion disapprobation conversion reaction.^[105] In symmetric cells and in full battery cells the anodic voltage will never reach such a high value.^[106,107] In asymmetric half-cells, a standard anodic cut-off limit of 1 V is also sufficient. Since Li₂Te does not decompose upon cycling, it is fundamentally different from alloy anodes as mentioned above.

The morphology and chemistry of the coating layer after the activation process were investigated using SEM, XRD, and

XPS. As shown in Figure S4, Supporting Information, the electrochemical reaction of Cu₂Te with Li to form Li₂Te leads to morphological changes in the film, although the layer remains ≈1 μm thick, per Figure 1i. The Te signal is correlated with S, P, and Cl signals. This is due to some decomposition of the argyrodite SE near 0 V versus Li/Li⁺ and the formation of S-, P-, and Cl-containing SEI. In addition, Cu is uniformly distributed throughout the interface, being a remnant of 2Li⁺ + 2e[−] + Cu₂Te ⇒ Li₂Te + 2Cu. Per Figure 1c, characteristic peaks of

Cu₂Te vanished after activation. Instead, the diffraction peaks appearing at 23.6°, 27.3°, 39.1°, 46.2°, 48.3°, and 62.0° are assigned to Li₂Te (JCPDS#23-0370). Figure 1d,e provides the high-resolution Te 3d and Cu 2p XPS spectra of the activated sample. The relative intensity of Cu⁰/Cu⁺ versus Cu²⁺ increases significantly as compared to that of the non-activated Cu₂Te layer (Figure S1, Supporting Information). This indicates that Li activation converts much of the Cu back to its metallic form. The Te remains in its reduced state with two peaks at 527.5 and 582.9 eV, respectively. As will be discussed throughout the manuscript, the resulting surface layer becomes an electrochemically stable mixture of these two interspersed phases. Upon lithium metal electrodisolution, it does not undergo a reversible conversion back to Cu₂Te but remains structurally stable both in the half-cells and in the full AF-ASSBs with an NMC cathode.

Following in situ Li activation, the PEEK half-cell is tested in a standard manner described in the experimental section and in the results below. The process is represented schematically in Figure 1f–h, with corresponding cross-sectional cryo-FIB-SEM images shown in Figure 1i–k. Per Figure 1i–k, the morphologically stable lithiophilic Li₂Te surface film facilitates Li wetting and uniform Li electrodeposition/electrodissolution. This in turn has significant influence on the electrochemical performance of the anode-free cells. The key properties of Li₂Te–Cu will be explored through combined experiments and modeling.

Galvanostatic electrodeposition/electrodissolution and EIS measurements of Li|SE|Li₂Te–Cu and baseline Li|SE|Cu half-cells were performed to understand the role of the Li₂Te current collector coating on the electrochemical properties of the cells. In all electrochemical tests conducted in this study an external pressure of 13 MPa was employed. Per Figure S5a, Supporting Information, tested at 0.5 mA cm⁻² the first-cycle

Li electrodeposition nucleation potential is 18 mV for Li₂Te–Cu and 44 mV for the Cu baseline. Per Figure S5b, Supporting Information, at 1 mA cm⁻², the first-cycle nucleation potential for Li₂Te–Cu is 25 mV, versus 58 mV for Cu. Figure S5c,d, Supporting Information, shows the galvanostatic electrodeposition profiles of these two samples at high current densities of 2 mA cm⁻² and above. With baseline Cu, during electrodeposition at 4 mA cm⁻² there is a sudden voltage drop prior to reaching the targeted 1 mAh cm⁻², indicating a short-circuit. At 5 mA cm⁻², the baseline Cu cell short-circuited at a capacity of only 0.2 mAh cm⁻². As will be demonstrated, incomplete wetting of electrodeposited Li on the Cu surface leads to a range of interfacial problems including current/electrical field focusing in the wetted areas (the electrochemically active interfacial area is lower than geometrical interfacial area), which leads to dendrite growth and ultimately to the observed electrical short-circuits. In contrast, the Li₂Te–Cu cell displays stable electrodeposition/electrodissolution profiles. The cells show no sign of short-circuiting even at a very high rate of 8 mA cm⁻², demonstrating a significant enhancement in the critical current density.

Figure 2a,b summarizes the nucleation (peak) overpotentials and mean electrodisolution overpotentials for Li₂Te–Cu and the baseline Cu current collectors at different current densities. As compared to Li₂Te–Cu, the baseline Cu provides a less favorable surface for Li electrodeposition, as evidenced by the higher nucleation potentials. With Li₂Te–Cu the lower nucleation overpotentials at every tested current density is indicative of its lithiophilicity. To further explore metal wetting behavior, “classic” molten Li wetting experiments were performed with the results being provided in Figure S6, Supporting Information. To summarize the approach: Lithium foil was melted on a stainless-steel plate inside the glovebox using a hotplate set

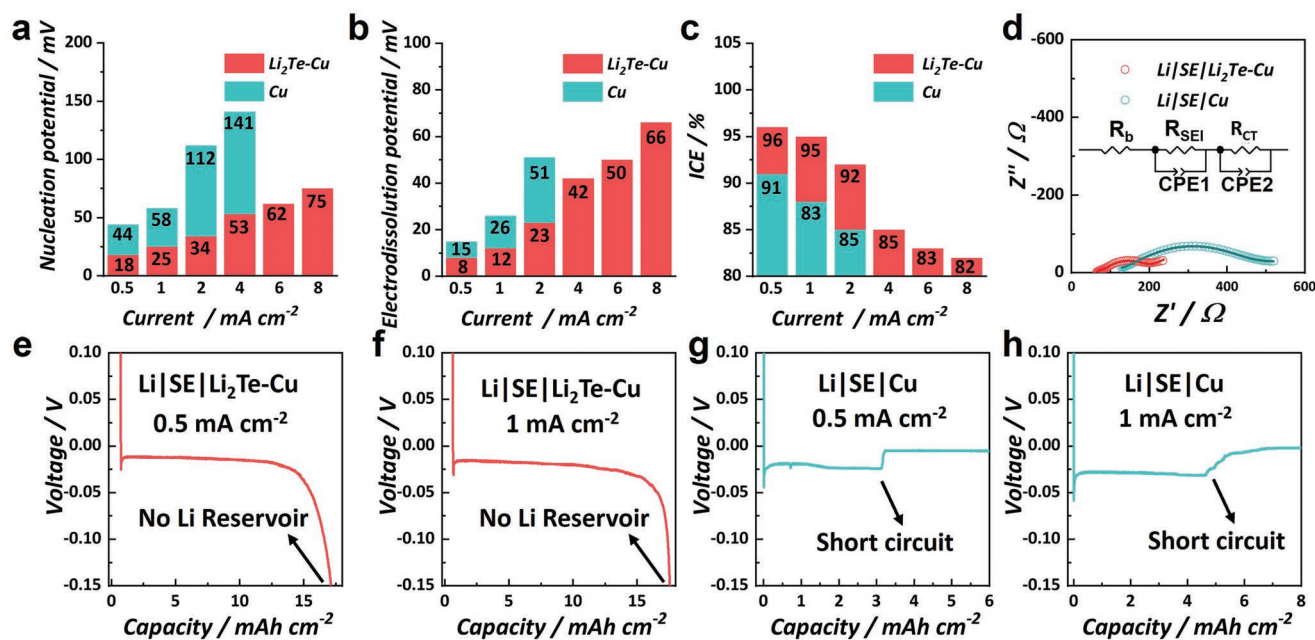


Figure 2. a) Nucleation potential, b) electrodisolution potential, and c) initial Coulombic efficiency (ICE) of Li|SE|Li₂Te–Cu and Li|SE|Cu cells at various current densities. d) Nyquist plots after electrodepositing 1 mAh cm⁻² Li at 0.5 mA cm⁻². Galvanostatic discharge profiles of e,f) Li|SE|Li₂Te–Cu and g,h) Li|SE|Cu at 0.5 and 1 mA cm⁻².

to 260 °C. The Te–Cu and baseline Cu foils were then dipped into the molten Li, the process being recorded with a camera. The difference in the thermal wetting behavior was stark; the molten Li uniformly wetted the surface of Te–Cu but poorly wetted baseline Cu. Such distinct thermal wetting characteristics may be correlated with electrochemical wetting as well. The interfacial energetics leading to such differences will be explored using atomic and mesoscale simulations, the results being presented later in the manuscript.

Interestingly the collector surface chemistry has an influence on the mean electrodissoolution overpotentials as well. As will be demonstrated, the chemistry of the underlying support influences the morphology of the electrodeposited metal and of the SEI. These factors will in turn affect the kinetics at which the complete electrodissoolution process occurs at every cycle. Figure 2c compares the initial Coulombic efficiency (ICE) of the samples tested at different current densities with a fixed electrodissoolution capacity of 1 mAh cm⁻². The Li₂Te–Cu cells displays ICEs of 96%, 95%, 92%, 85%, 83%, and 82% at current densities of 0.5, 1, 2, 4, 6, and 8 mA cm⁻². The baseline Cu cell exhibits much lower ICEs of 91%, 88%, and 85% at 0.5, 1, and 2 mA cm⁻², while the cells appear to short-circuit at higher rates. Figure 2d displays the Nyquist plots of the two specimens after electrodepositing a capacity of 1 mAh cm⁻² Li at 0.5 mA cm⁻². Both plots are fitted by an equivalent circuit composed of a bulk resistance R_b and SEI resistance R_{SEI} (higher frequency) in series with a parallel connection of a constant phase element CPE1 and a charge transfer resistance R_{CT} in series with a parallel connection of CPE2. The two semicircles overlap with the combined R_{SEI} and R_{CT} being 62 Ω for Li₂Te–Cu and 360 Ω for baseline Cu.

To examine the utility of Li₂Te–Cu supports for high mass loading cathode applications, continuous Li electrodeposition tests were performed. Figure 2e–h shows these results, where Li was continuously electrodeposited on the two substrates. At a current density of 0.5 mA cm⁻², 3.1 mAh cm⁻² of Li can be electrodeposited on the baseline Cu foil with a short-circuit occurring afterward. At 1 mA cm⁻², the voltage abruptly dropped after accumulating 4.5 mAh cm⁻² capacity. For the Li₂Te–Cu cells, stable electrodeposition profiles are maintained for over 15 mAh cm⁻² at both current densities. The point where the voltage starts to increase is ascribed to the exhaustion of the Li on the counter electrode. The accumulated thickness of electrodeposited Li on Li₂Te–Cu is calculated to be more than 70 μm, which matches the thickness of the Li foil counter-electrode. In contrast, the allowable amount of Li deposited on baseline Cu foil is less than 20 μm.

Figure 3a–h displays the electrochemical performance results of Li₂Te–Cu and identically tested baseline Cu half-cells. Figure 3a,b compares the Coulombic efficiencies (CEs) during the initial Li electrodeposition/electrodissoolution process. The tests were carried out according to the standard protocol reported previously for evaluating the efficiency of Li cycling, per refs.[108,109] An initial formation cycle was performed at 0.5 mA cm⁻² to a capacity of 5 mAh cm⁻², followed by electrodissoolution at the same current to an anodic limit of 1 V versus Li/Li⁺. This was followed by electrodepositing a 5 mAh cm⁻² Li reservoir at 0.5 mA cm⁻², followed by ten cycles of electrodeposition/electrodissoolution (from that reservoir) of

0.5 mAh cm⁻² at 0.5 mA cm⁻². The last step in the test was electrodissoolution of the entire reservoir at 0.5 mA cm⁻² to the 1 V anodic limit. The final measured CE for the entire process with Li₂Te–Cu and with baseline Cu was 99.70% and 98.47%, respectively. The difference in the CEs between the two specimens can be explained in terms of a combination of SEI growth from the reaction of the SE with the Li metal and the formation of electrochemically inactive dead-metal on the collector surface. Both factors were more extreme for the baseline Cu, as will be demonstrated by microstructural analysis.

The cycling performance of Li₂Te–Cu and baseline Cu half-cells is shown in Figure 3c–h. The figures display tests at 0.1 mA cm⁻² to 1 mAh cm⁻² and 0.5 mA cm⁻² to 1 mAh cm⁻², respectively. In each row, the smaller second and third panels are the enlarged profiles of selected regions in the first larger panel. With these asymmetric configurations there is no “extra” Li reservoir employed. Since the CE is never 100%, an anodic voltage of 1 V is employed, after which point the current is reversed. Significant differences in the voltage–time profiles are evident at both current densities. For baseline Cu tested at 0.1 mA cm⁻² to 1 mAh cm⁻², the profile begins to substantially deteriorate from the third cycle onward. This is illustrated in Figure 3d. By contrast, the Li₂Te–Cu cell exhibits stable electrodeposition and electrodissoolution for up to 650 h, corresponding to 32 cycles. These results are shown in Figure 3e. According to Figure 3f–h, the baseline Cu tested at 0.5 mA cm⁻² became unstable starting from the 12th cycle (43 h). The Li₂Te–Cu, however, can stably cycle more than 380 h at this current. Figure S7, Supporting Information, displays the cycling data at 0.5 mA cm⁻² but with a more critical capacity of 3 mAh cm⁻² being electrodeposited starting from the second cycle, corresponding to a high areal loading cathode in practical applications. The profile of baseline Cu becomes unstable from the fifth cycle, finally shorted after seven cycles. By contrast, the Li₂Te–Cu cell remains stable for up to 200 h without any signs of deterioration. Figure S8, Supporting Information, compares the Li₂Te–Cu cells with different Cu₂Te mass loadings, 0.1 and 1 mg cm⁻². It may be observed that in both cases the galvanostatic profiles deteriorated at earlier, starting from 44 h at 0.1 mg cm⁻² and 122 h at 1 mg cm⁻². While the cause of the inferior performance in both cases was not investigated in detail, it may be surmised that at the extremely low mass loading the surface coverage by the Cu₂Te may be incomplete, while at the higher mass loading the layer may peel off during cycling. Therefore, all electroanalytical and analytical studies in this manuscript are based on the Li₂Te–Cu with 0.4 mg cm⁻², unless otherwise indicated.

Figure S9, Supporting Information, shows the top-down SEM and EDXS images illustrating the surface morphology of Li₂Te–Cu and of the SE after cycling 100 times to 1 mAh cm⁻² at 0.5 mA cm⁻² (after the last electrodissoolution cycle, the cell was physically separated for imaging). The Li₂Te–Cu collector surface retains its roughened morphology, while the SE surface remains relatively smooth and uniform. Figure S10, Supporting Information, provides the XPS analysis on the surface of Li₂Te–Cu after cycling 20 times to 1 mAh cm⁻² at 0.5 mA cm⁻². Comparing with Figure S1c, Supporting Information, it may be observed that there are minimal binding energy changes for the Te and Cu elements (stable Li₂Te and reduced Cu) as compared

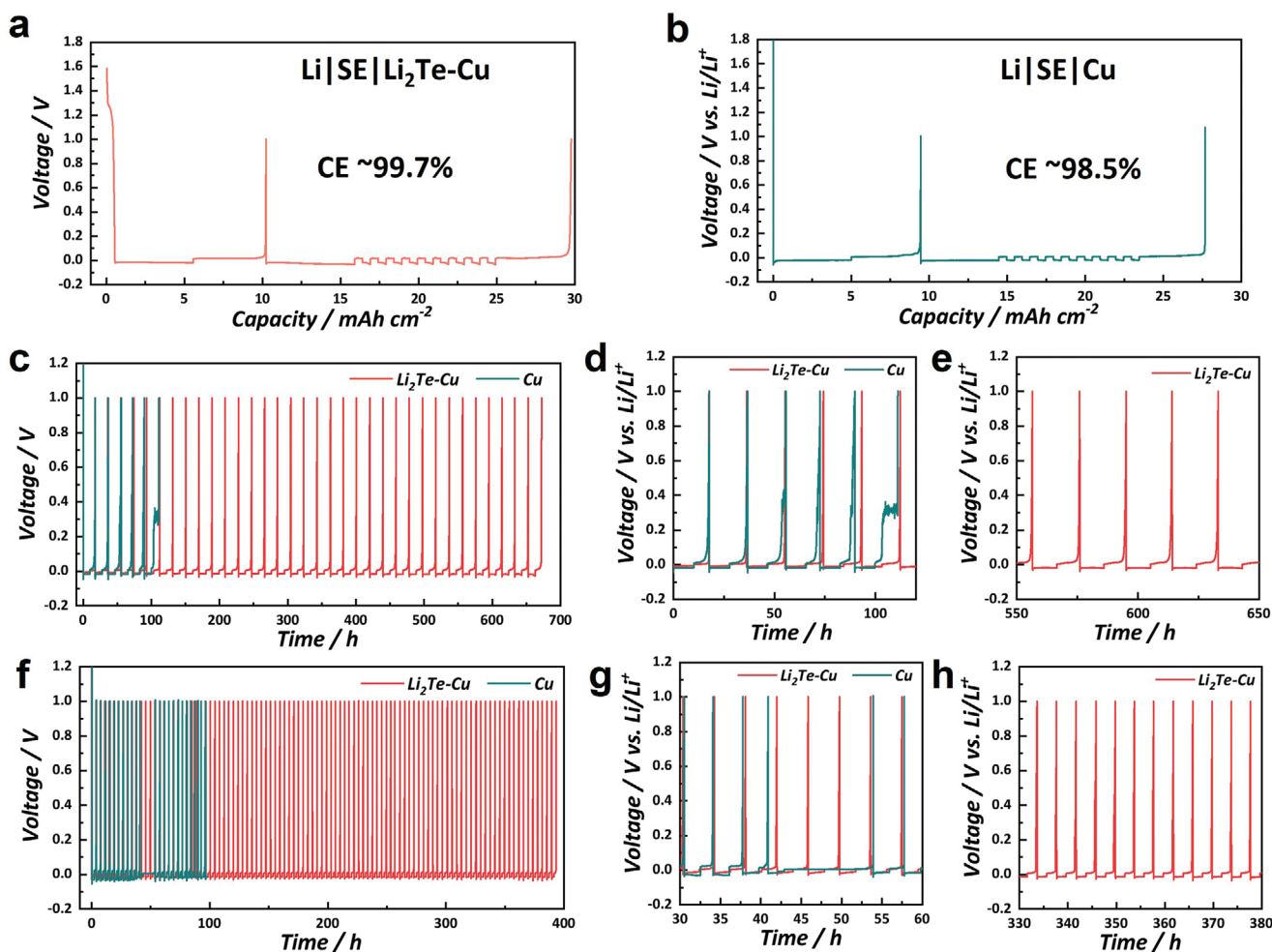


Figure 3. Coulombic efficiency measurement of a) Li|SE|Li₂Te–Cu and b) Li|SE|Cu cells. Galvanostatic cycling performance of Li|SE|Li₂Te–Cu and Li|SE|Cu cells tested at c–e) 0.1 mA cm^{−2} and f–h) 0.5 mA cm^{−2} to a fixed electrodeposition capacity of 1 mAh cm^{−2}.

with their state directly after activation. Per Figure S10a, Supporting Information, the peaks corresponding to Te^{2−} 3d_{5/2} (572.4 eV) and Te^{2−} 3d_{3/2} (582.8 eV) can be observed along with Cu LMM Auger. The peaks at 931.8 and 951.5 eV can be assigned to Cu⁰/Cu⁺ 2p_{3/2} and Cu⁰/Cu⁺ 2p_{1/2}, while the peaks at 932.8 and 952.5 eV are ascribed to Cu²⁺ 2p_{3/2} and Cu²⁺ 2p_{1/2}. Those results are presented in Figure S10b, Supporting Information.

Figure 4 presents cross-sectional cryo-FIB SEM and EDXS-based microstructural analysis of post-electrodeposited and of post-electrodissolved Li₂Te–Cu cells. All the testing was performed at 0.5 mA cm^{−2}. Figure 4a–c displays the cell microstructure after electrodeposition of 1 mAh cm^{−2}. Figure 4d–f displays the microstructure after electrodeposition of 3 mAh cm^{−2}. Figure 4g–i shows it after electrodeposition of 5 mAh cm^{−2}. Figure 4j–l shows the microstructure after electro-dissolving 3 mAh cm^{−2} to a remnant capacity of 2 mAh cm^{−2}. Finally Figure 4m–o displays the microstructure after electro-dissolving the remaining Li to the 1 V anodic limit. A key unifying observation is that the electrodeposited Li on the Li₂Te–Cu collector is dense and uniform. At accumulated capacities of 1, 3, and 5 mAh cm^{−2}, the measured metal thicknesses are 4.2,

13.3, and 23.8 μm. These values are incrementally lower than the theoretical values of 4.9, 14.1, and 24.5 μm respectively. This can be attributed to the role of cell pressure that results in creep deformation of the metal, causing it to slightly thin in the direction parallel to the applied stress and correspondingly widen in the normal direction.^[110]

With Li₂Te–Cu, it may be observed that the electrodeposited Li metal is largely pore-free and does not contain appreciable embedded SEI. This Li microstructure is consistent after accumulating capacities of 3 and 5 mAh cm^{−2}, and after subsequent electro-dissolving of 3 mAh cm^{−2} of this capacity. In this terminally electro-dissolved state there is no evidence of dead metal left on the Li₂Te–Cu surface, while the Li₂Te layer is continuous and relatively undistorted. According to Figure 4n and Figure S11, Supporting Information, it may be observed that after complete electro-dissolution, the remnant Li₂Te–Cu surface consists of interspersed Li₂Te and Cu phases, each having a roughly spherical morphology. The Li₂Te and Cu remain intact after Li electro-dissolution and Cu₂Te is not re-formed, per previously discussed electroanalysis, SEM, and, XPS results. In every observable way, the post-Li electro-dissolution Li₂Te–Cu surface is analogous to what it was directly after the initial activation

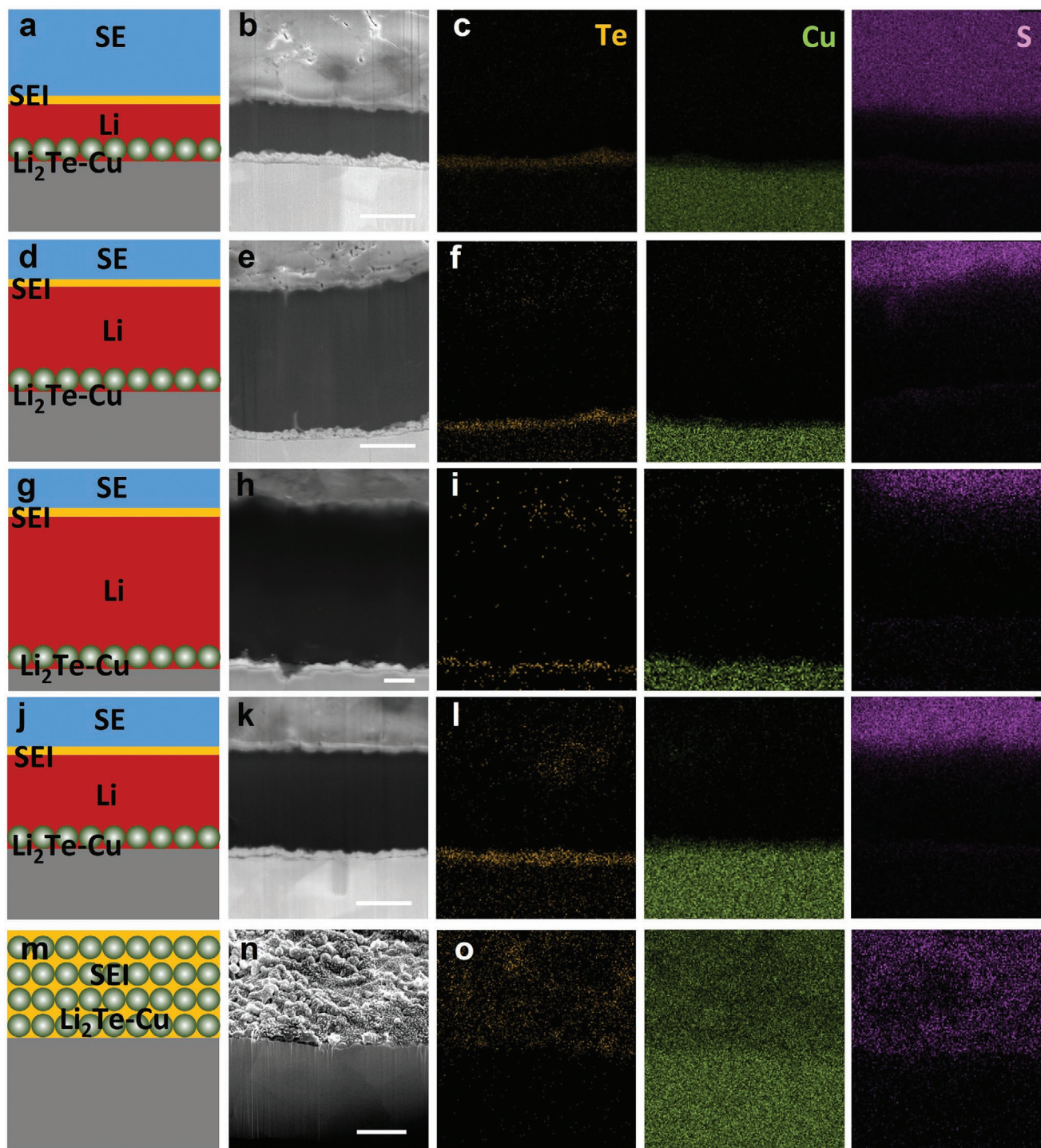


Figure 4. Cryo-FIB cross-sectional SEM and EDXS of the Li|SE|Li₂Te-Cu cell, tested at 0.5 mA cm⁻² a-c) electrodeposition of 1 mAh cm⁻², d-f) electrodeposition of 3 mAh cm⁻², g-i) electrodeposition of 5 mAh cm⁻², j-l) electrodis-solution of 3 mAh cm⁻², and m-o) electrodis-solution to 1.0 V. The scale bar is 5 μm.

step. Moreover, according to top-down SEM images shown in Figure S11, Supporting Information, in this fully electrodis-solved state the current collector is easily detached from the SE with the two interfaces remaining intact. The EDXS indicates that the top surface layer is mainly composed of Li₂Te and Cu, along with some SE residues. A weak Pt signal is also detected,

which was ascribed to the sputter deposited Pt that was used to enhance the electronic conductivity of the sample allowing for cryo-EM analysis without charging.

Figure 5a-h displays an analysis of the baseline Cu substrate after one electrodeposition/electrodis-solution cycle, to a capacity of 1 mAh cm⁻² at 0.5 mA cm⁻². Figure 5a shows the

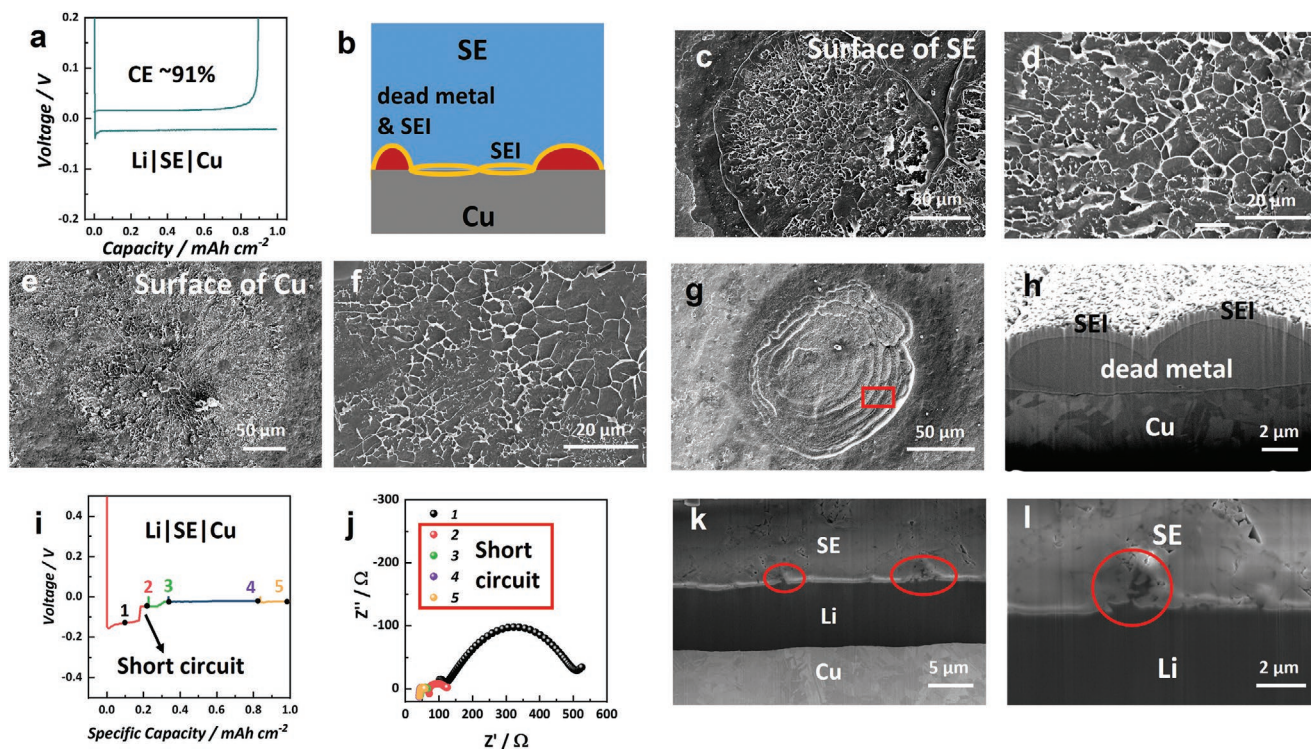


Figure 5. a) Galvanostatic profile of the Li|SE|Cu cell with capacity of 1 mAh cm^{-2} , tested at 0.5 mA cm^{-2} . b) Schematic of the Li|SE|Cu cell at electro-dissolved state with honeycomb-like SEI and dead metal remaining. c, d) Top-down SEM images of SEI in the separated cell showing SE surface. e, f) Same analysis of the Cu surface (not same area). g, h) Top-down and cryo-FIB SEM cross-sectional images of electrochemically inactive dead-metal on electro-dissolved surface. i, j) Galvanostatic electro-deposition curve and corresponding EIS plots at 3 mA cm^{-2} to 1 mAh cm^{-2} at cycle 1. k, l) cryo-FIB cross-sectional SEM images of interface containing metal dendrites (circled) propagating into the SE, after electro-deposition of 3 mAh cm^{-2} .

galvanostatic charge/discharge (GCD) profile of the baseline Cu cell tested at 0.5 mA cm^{-2} . The ICE of the baseline Cu cell is 91% versus 96% measured for $\text{Li}_2\text{Te}-\text{Cu}$. As the next set of panels illustrates, this difference is due to extensive and irregular SEI formation and the presence of electrochemically inactive dead metal on the baseline Cu. A schematic illustration of the Li|SE|Cu cell after Li electro-dissolution is shown in Figure 5b, highlighting these two critical deleterious features of the electro-dissolved interface. Figure 5c–f displays the top-down SEM images of the electro-dissolved surface of SE and the Cu collector, respectively. A key feature of both interfaces is the islands of honeycomb-like SEI that remain on both surfaces. These islands possess a diameter in the $100\text{--}200 \mu\text{m}$ range and are caused by the reaction between the SE and the Li metal. The known reaction products between LPSCl and Li include stable Li_2S , Li_3P , and LiCl , as well as several metastable phases including Li_3PS_4 , S, P, and P_2S_5 .^[52,111] The fact that the SEI has the shape of islands indicates that the Li metal is not fully wetted on the Cu current collector, as otherwise the SEI would be continuous across the surfaces. The SEI appears to be adherent to both Cu and SE, with the circular islands being relatively whole on both surfaces.

Figure S12, Supporting Information, shows top-down SEM results of the baseline Cu after electro-depositing 1 mAh cm^{-2} of Li at 0.5 mA cm^{-2} . It may be observed that at this current density the Li metal is poorly wetted on the Cu support, with several isolated islands of Li bridging the collector to the SE. The

incompletely wetted Li on the Cu collector leads to a localized increase in the current density and electrical field focusing due to reduced effective cross-sectional area over which the current is distributed. This should in turn promote accelerated SE decomposition, as well as enhanced metal dendrite growth per the well-established theory. One straightforward effect of a decreased electroactive surface area due to poor metal wetting on the current collector is to increase the electrical and ionic current density during charging–discharging. Established continuum-based models that treat ion concentration effect in liquid electrolyte solution shed light on how this destabilizes the electrolyte metal interphase. For example, the classic model by Newman et al. considered a tip of a dendrite with high curvature and how this intensifies the local electric field, a process that would be equally applicable to the SE–metal interface. The increased current density would drive further metal electro-deposition making the process self-amplifying.^[86,88] For the argyrodite SE–metal interface, there are also a series of equilibrium and metastable reduction decomposition reactions, discussed previously. As with any redox process, these decomposition reactions display Tafel behavior with a locally increased current density accelerating the process.

Figure 5g presents top-down SEM images highlighting the irregular surface of the electro-dissolved Cu with circular island-like features on the $100\text{--}200 \mu\text{m}$ scale. Figure 5h displays the cross-sectional cryo-FIB SEM image of the selected area in Figure 5g. According to Figure 5g, on the electro-dissolved Cu

surface there is non-dissolved dead Li metal with droplet-like morphology (further supporting the poor-wetting scenario). The dead metal, along with the extensive SEI, are the two key features explaining the low CE observed for the baseline Cu. These two undesirable microstructural features are not detected for the Li_2Te -Cu specimens in the electrodisolved state. As shown by the EDXS maps in Figure S13, Supporting Information, the dead metal is also covered by a thick SEI layer that can be readily distinguished by its chemical features.

Figure 5k,l shows the cross-sectional cryo-FIB SEM images of the Li deposited to a capacity of 3 mAh cm^{-2} at 0.5 mA cm^{-2} . Both sets of analyses, performed on different wetted portions of the Li metal, demonstrate dendrites protruding into the SE. The images are presented at a lower and a higher magnification to illustrate both the general morphology of the interface and the specific morphology of a single-branched dendrite. Figure 5i,j shows the galvanostatic electrodeposition curve and corresponding EIS Nyquist plots for baseline Cu tested at 3 mA cm^{-2} . Figure S14, Supporting Information, shows these Nyquist plots at higher resolution. At this high current, a short-circuit occurs after depositing a capacity of $\approx 0.2 \text{ mAh cm}^{-2}$. This is evident by both the sharp drop in the overpotential during electrodeposition (due to the onset of mixed electron-ion conduction) and a sharp decrease in the cell impedance for the same reason.

The electrodeposition behavior of Li on the Li_2Te -Cu and baseline Cu surfaces was further investigated with DFT calculations. If Li clusters are more thermodynamically stable than individual Li atoms, early-stage wetting behavior will favor 3D islands rather than atomically thin continuous films. This would naturally lead to dendrites as the film thickness increases. If Li atoms are more stable as compared to Li clusters, the initially electrodeposited film will cover the surface uniformly. It should be cautioned that these thermodynamic results don't address the kinetic factors that will also influence the electrodeposition morphology, such as the heterogeneity of the Li-ion flux through the formed SEI or through the argyrodite SE that is not 100% dense. For example, per the FIB analysis, with the baseline Cu supports the SEI is much more geometrically heterogeneous than with Li_2Te -Cu supports.

The binding energies of Li atoms and Li clusters on the (110) fcc Li_2Te surface were calculated and compared to (111) fcc Cu and (110) bcc Li. The binding energies were calculated in two configurations: 1) Li clusters and 2) individual Li atoms. The structures of Li_4/Li_5 clusters and four/five individual Li atoms on the respective surfaces are shown in Figures S15 and S16, Supporting Information. The binding energies of the Li_4 cluster, Li_5 cluster, four and five Li atoms are shown in Table 1. Outcomes with the lowest binding energy with respect to other

configurations are the most thermodynamically stable. As discussed, a higher thermodynamic stability of individual Li atoms as compared to clusters indicates the propensity to grow uniformly on a given surface. A key comparison is for the energy differences within each class of supports, in addition to a cross-comparison between the classes. Three cross-comparisons should be made: The energy of clusters versus metal atoms on a (111) fcc Cu surface, the energy of clusters versus metal atoms on (110) bcc Li surface, and the energy of clusters versus metal atoms on (110) fcc Li_2Te surface.

It may be observed that on Cu (111) surface, the four Li atoms and Li_4 clusters are almost equally stable, both binding strongly to the Cu support. Five Li atoms and Li_5 clusters are also strongly bound to the support. However, since five atoms are more stable with lower binding energy, the first electrodeposited monolayer should be conformal and would not dewet the Cu surface. The binding energy of Li atoms and of Li clusters on (110) fcc Li_2Te is significantly weaker than on (111) fcc Cu. This implies that if there were regions of exposed Cu support in the Li_2Te -Cu specimens, the first monolayer of Li may preferentially wet there. Per the cross-sectional and top-down FIB SEM results, the tellurium thermal deposition process appears quite conformal, making this scenario unlikely except in isolated regions that are out of the field of view. Examining the energy values within the (110) fcc Li_2Te row it may be observed that four and five Li atoms are more stable than the clusters. This indicates that there is a thermodynamic driving force for complete monolayer coverage of the Li_2Te -Cu support, akin to the baseline Cu. Interestingly, on pre-existing (110) bcc Li the Li atoms are less stable than the clusters. This implies a thermodynamic propensity for roughening of the Li metal surface during ongoing film growth. This scenario indicates the possibility of Stranski-Krastanov type dewetting during electrodeposition. One could reasonably surmise that the external pressure on the cells aids in suppressing such instabilities at later stages of electrodeposition. Thermodynamic propensity of Li to roughen as it electrodeposits on pre-existing metal may also be a reason why it is near-universally reported that significant external pressure is necessary to achieve stable cycling with SEs.

While Li can bind strongly to a neat surface and wet it, subsequent binding can be weaker on the now-passivated surface, leading to dewetted islands and ultimately to dendrites. To further understand the continuous Li electrodeposition on the three supports, binding energy calculations were performed on bilayers, consisting of a monolayer (ML) of Li on top of (111) fcc Cu, (110) bcc Li, or (110) fcc Li_2Te . The atoms versus clusters methodology followed an analogous approach, but with ML of Li being introduced on top of the relevant surfaces. This is shown in Figure 6. The binding of Li on the Li-ML-covered surface was calculated and is shown in Table 2. The enhancement of relative stability of Li clusters versus Li atoms on (110) bcc Li surface agrees with the results shown in Table 1, and further highlights the thermodynamic instability of a growing Li front per se. Again, this may be a key reason why significant external pressure seems necessary to prevent dendrites regardless of the type of SE employed. Another key observation is the significant weakening of Li binding to the Li-covered (111) Cu surface. While a monolayer of Li is very adherent to Cu, the adhesion is greatly diminished with a bilayer. In contrast, there

Table 1. Binding energies for multiple lithium atoms and lithium clusters on the relevant surfaces.

Binding Energy per Li [eV]	Four Li atoms	Li_4 cluster	Five Li atoms	Li_5 cluster
(111) fcc Cu	-0.570	-0.560	-0.531	-0.320
(110) bcc Li	0.168	0.121	0.188	0.111
(110) fcc Li_2Te	0.535	0.630	0.538	0.595

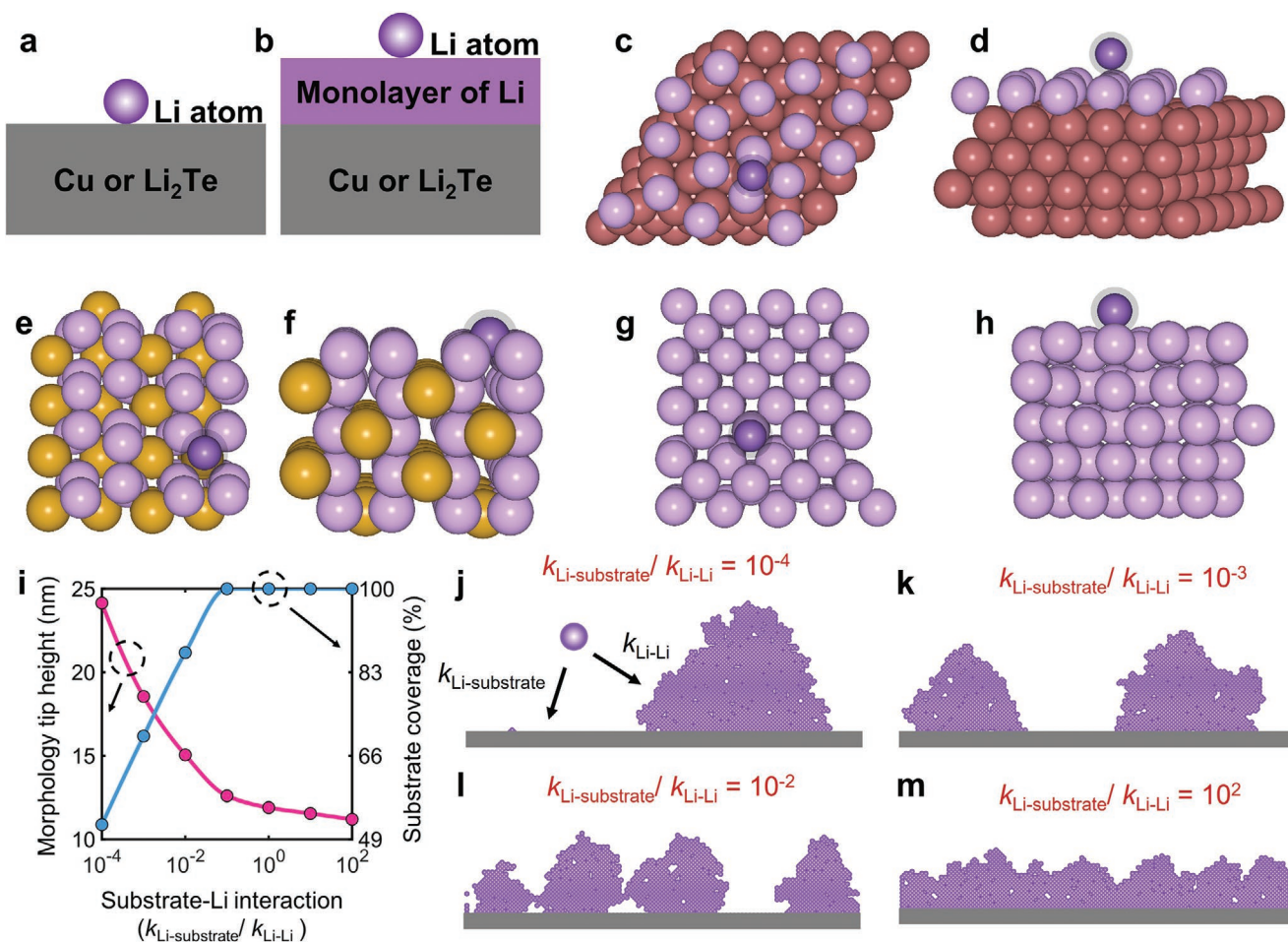


Figure 6. a,b) Schematics and representative atomic structures of one Li atom or a monolayer of Li on top of c,d) fcc Cu, e,f) fcc Li₂Te, and g,h) bcc Li surfaces. Color scheme: Li (pink), Te (yellow), Cu (brown), and Li in binding site (purple). i) Morphology tip height and substrate coverage as a function of the substrate–Li interaction. j–m) Effect of substrate–Li interaction on the nucleation behavior and morphological evolution.

is a significant strengthening of Li binding to the (111) fcc Li₂Te after one monolayer is deposited. Furthermore, after two Li monolayers are deposited on the surface, the binding energy of the Li atom decreases in (110) fcc Li₂Te while increasing in (111) fcc Cu, as shown in Table 2. This indicates the presence of subsurface effects from Li₂Te and validates the experimentally observed potency of the Li₂Te–Cu support. It is perhaps the most meaningful outcome of the simulation, providing insight into how Li₂Te guides lithium growth beyond a single atomic layer.

To understand the morphological growth during Li electrodeposition, we developed a mesoscale model based on the

Table 2. Binding energies of a single lithium on the relevant surfaces and on one or two lithium monolayers.

	Binding energy per Li on the surface [eV]	Binding energy per Li on a Li monolayer [eV]	Binding energy per Li on two Li monolayers [eV]
(111) fcc Cu	−0.570	0.088	0.108
(110) bcc Li	0.116	0.182	—
(110) fcc Li ₂ Te	0.537	0.077	−0.025

kinetic Monte Carlo approach that captures the competing effect of Li's binding behavior on the substrate and Li's binding behavior on freshly deposited Li on the substrate.^[112–114] This competing interaction (Figure 6i) is described using $k_{\text{Li-substrate}}/k_{\text{Li-Li}}$, where $k_{\text{Li-substrate}}$ describes the adsorption kinetics of Li on the substrate and $k_{\text{Li-Li}}$ describes the adsorption kinetics of Li on newly deposited Li. A detailed description of the mesoscale modeling framework has been presented in the Computational Details section. The underpinning Li–substrate interaction affects the Li nuclei coverage over the substrate and subsequent electrochemical growth of these morphologies. We note that these simulations to analyze the nucleation and early growth morphologies have been performed until a total of 2000 atoms have been deposited. As shown in Figure 6i, an increase in $k_{\text{Li-substrate}}/k_{\text{Li-Li}}$ results in a significant improvement in the substrate utilization, attributed to the preferential coverage of Li on the substrate. This effect promotes higher uniformity in flux distribution for subsequent electrochemical growth of the nuclei. As a function of the $k_{\text{Li-substrate}}/k_{\text{Li-Li}}$ descriptor, Figure 6j–m shows the early growth behavior, highlighting the prominent difference in nuclei coverage and morphological patterns. As illustrated in Figure 6i–m, a stronger

substrate–Li interaction also results in homogenized deposition, accompanied by a reduction in tip height of these morphologies. Overall, the mechanistic insights from the DFT calculations and the mesoscale model highlight the fundamental role of the substrate–metal interaction on the morphological behavior, corroborating the critical effect of Li_2Te that is experimentally observed in enabling stable electrodeposition.

As proof-of-principle, anode-free all-solid-state batteries (AF-ASSB) were fabricated and tested using with Li_2Te –Cu or baseline Cu. For AF-ASSB there is no active ion reservoir apart from what is in the cathode, CEs approaching 100% are crucial. The cells were based on $\text{LiNi}_{0.8}\text{Mn}_{0.1}\text{Co}_{0.1}\text{O}_2$ (NMC811) cathodes and argyrodite LPSCl electrolyte. The CEs in the AF-ASSBs are calculated based on the discharge and charge capacities of the NMC cathodes. Both Li_2Te –Cu and baseline Cu anode current collectors were analyzed with the same cathode formulation and loading. **Figure 7a** illustrates the working principle of the Li_2Te –Cu|SE|NMC cell. **Figure 7b** shows the cryo-FIB SEM analysis of the cathode structure where NMC is mixed with SE to achieve sufficient ionic flux. No carbon additives were employed to construct the cathode architectures. **Figure 7c,d** presents the EDXS maps that indicate homogenous mixing of the cathode active material and the SE. **Figure 7e** displays the first cycle galvanostatic profiles of Li_2Te –Cu|SE|NMC and Cu|SE|NMC cells at a current density of 0.2C (1C equals to 200 mA g^{-1} based on the mass of NMC). It may be observed

that small plateaus are present in the Li_2Te –Cu|SE|NMC full cell at voltages of ≈ 2.3 and 2.5 V with an overall capacity of $\approx 25 \text{ mAh g}^{-1}$, corresponding to the activation between Cu_2Te and Li (details in Note S1, Supporting Information). This corresponds to the in situ reaction between Cu_2Te and Li to form Li_2Te and Cu, per **Figure 1b**. The kinetically irreversible reaction to form Li_2Te occurs only on the initial charge cycle. Neither the subsequent discharge nor the following charge cycles display the plateau. The Li_2Te –Cu|SE|NMC cell exhibits initial charge and discharge capacities of 199 and 165 mAh g^{-1} , corresponding to an ICE of 83%. By contrast, the Cu|SE|NMC cell delivered 208 and 151 mAh g^{-1} , corresponding to an ICE of 72%. The increased CE of Li_2Te –Cu|SE|NMC is directly attributed to the lithiophilic Li_2Te –Cu surface.

Figure S17, Supporting Information, displays the cyclic voltammetry profiles of Li_2Te –Cu|SE|NMC and Cu|SE|NMC cells, tested at a scan rate of 0.1 mV s^{-1} . For Li_2Te –Cu|SE|NMC, two overlapping anodic peaks at 2.3 and 2.5 V are present during the initial charge process. These correspond to the irreversible conversion of Cu_2Te to Li_2Te and Cu, the position of the peaks being consistent with the Li activation results discussed earlier. The oxidation peak at 4.13 V is attributed to the delithiation of NMC, which subsequently shifts to 3.96 and 3.97 V during the subsequent cycles. By contrast, the baseline Cu|SE|NMC cell only exhibits one oxidation peak at 4.20 V, which subsequently shifts to 4.04 and 4.06 V. The higher delithiation potentials of

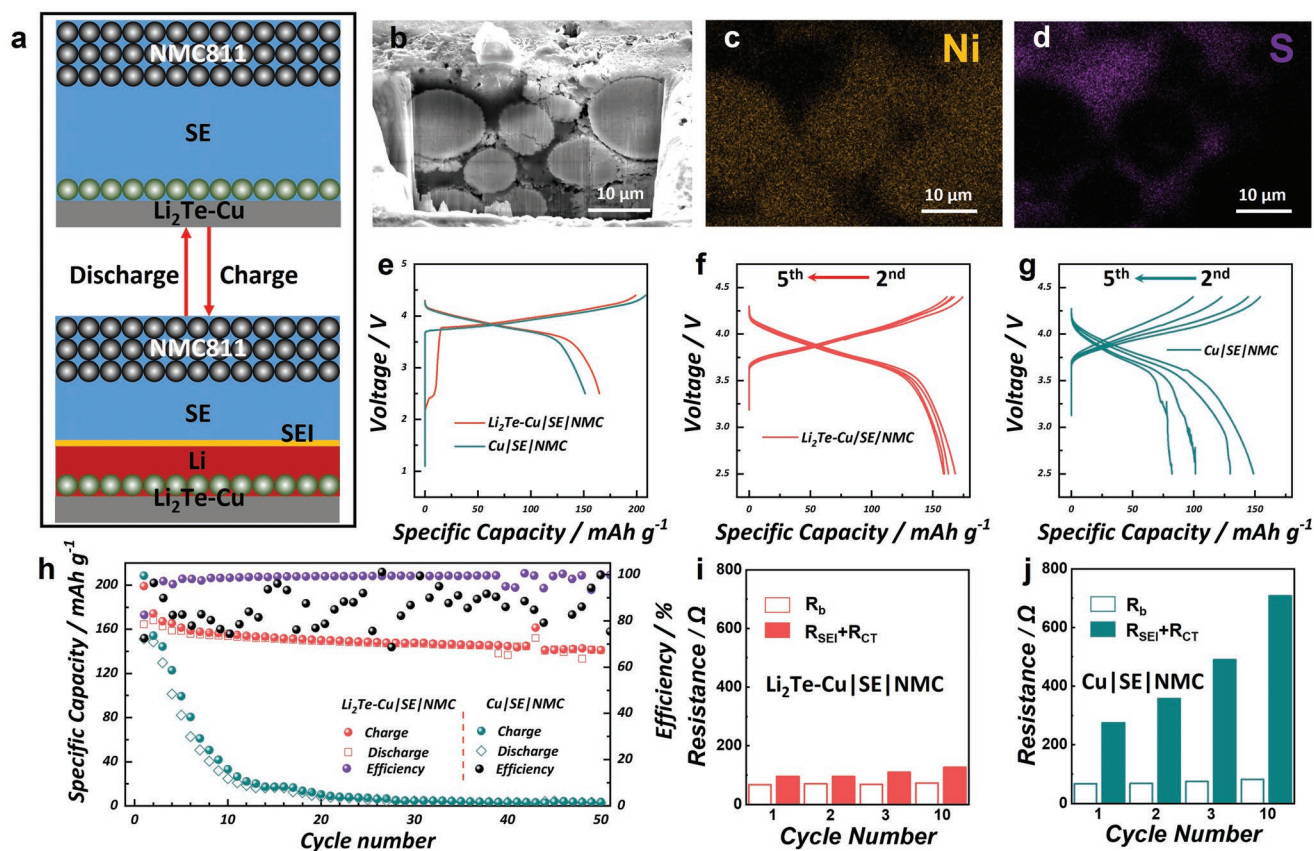


Figure 7. a) Schematic diagram of the working principle in an anode-free solid-state battery. b–d) Cryo-FIB SEM images and EDXS maps of the NMC cathode intermixed with the SE. e–g) Galvanostatic charge/discharge profiles at 1st cycle and 2nd–5th cycle. h) Cycling performance of Li_2Te –Cu|SE|NMC and Cu|SE|NMC cells and i, j) results of the EIS analysis of the two specimens at different stages of cycling.

the Cu|SE|NMC indicate higher overpotentials/polarizations during Li electrodeposition on the anode collectors, which again agrees with the half-cell data.

Figure 7f,g compares the galvanostatic profiles of $\text{Li}_2\text{Te-Cu|SE|NMC}$ and Cu|SE|NMC cells in the subsequent cycles. It may be observed that the Cu|SE|NMC cell undergoes a significant capacity decay at each cycle, with capacities of 148, 130, 101, and 83 mAh g^{-1} at cycles 2–5. The cell's voltage–capacity profile begins to notably deteriorate from the third discharge onwards. By contrast, the $\text{Li}_2\text{Te-Cu|SE|NMC}$ cells exhibit relatively stable charge/discharge profiles and deliver reversible capacities of 168, 163, 159, and 159 mAh g^{-1} at cycles 2–5. Figure 7h contrasts the cycling performance of $\text{Li}_2\text{Te-Cu|SE|NMC}$ and Cu|SE|NMC cells. A substantial capacity decay can be found with the Cu|SE|NMC cell with 33 mAh g^{-1} being sustained after ten cycles and nil capacity soon afterward. The $\text{Li}_2\text{Te-Cu|SE|NMC}$ cell exhibits more stable cycling with a capacity retention of 80% after 50 cycles and an average CE above 99%.

Figure S18a,c, Supporting Information, displays the extended cycling of the $\text{Li}_2\text{Te-Cu|SE|NMC}$ cells and the CE starts to fluctuate starting from the 57th cycle onwards. From the presented 62nd to 64th cycle charge–discharge profiles, this deterioration may be associated with high voltage instability, that is, a process occurring most likely at the cathode. To explicitly explore the role of NMC cathode degradation in the lifetime of $\text{Li}_2\text{Te-Cu|SE|NMC}$ cells, a “conventional” ASSB with a standard thick Li metal foil anode was fabricated and tested. In this case there is an effectively infinite reservoir of Li and the electrodeposition–electrodissolution always takes place on a pre-existing Li metal surface. There is never an empty current collector. That specimen is labeled Li|SE|NMC and was tested identically to the $\text{Li}_2\text{Te-Cu|SE|NMC}$. Those side-by-side comparison results are shown in Figure S18b,d, Supporting Information. With Li|SE|NMC a similar deterioration process is observed, Li|SE|NMC becomes unstable after the 67th cycle. As there is always sufficient Li available at the anode so Li depletion per se cannot be the culprit. According to previous studies, the LPSCl SE also decomposes at the interface with cathode electrodes, being oxidized into elemental S, lithium polysulfides, and phosphates.^[115] In addition, NMC polycrystalline particles undergo volumetric strain during lithium intercalation/extraction.^[116] Upon charging, lithium is extracted from NMC811, which may cause contact loss between SE and NMC, increasing the charge transfer resistance and the irreversible capacity.^[49] After repeated cycling, the NMC polycrystalline particles may become pulverized because of the stress vibration from the phase transitions leading to the internal microcracks growing to the surface.^[117] All these could account for the unstable cycling of AF-ASSB $\text{Li}_2\text{Te-Cu|SE|NMC}$ cells. Authors have mitigated such SE-cathode-related issues by employing single-crystal NMC^[118] or coating the NMC surface with Li-containing compounds such as LiNbO_3 ,^[119,120] Li_2ZrO_3 ,^[121] and Li_2SiO_3 .^[122] This study, however, focused on current collector–metal anode–SE interrelations, and a standard commercial NMC811 cathode was employed.

Figure S19, Supporting Information, shows the rate capability of $\text{Li}_2\text{Te-Cu|SE|NMC}$, with discharge capacities of 193, 121, and 103 mAh g^{-1} being obtained at 0.1, 0.5, and 1C. Figure 7i,j

and Figure S20, Supporting Information, display the electrochemical impedance behaviors of both $\text{Li}_2\text{Te-Cu|SE|NMC}$ and Cu|SE|NMC cells after charging at different cycles. Both plots are fit to an equivalent circuit composed of an R_b and overlapped $R_{\text{SEI}}+R_{\text{CT}}$ in series with a parallel connection of CPE. The $R_{\text{SEI}}+R_{\text{CT}}$ value of the first, second, third, and tenth charging was 95, 95, 110, and 126 Ω for $\text{Li}_2\text{Te-Cu|SE|NMC}$, and 275, 358, 490, and 708 Ω for Cu|SE|NMC . Overall, these AF-ASSB results agree well with the analytical and electroanalytical findings for the half-cells.

3. Conclusions

We report an AF-ASSB employing a sulfide-based solid-electrolyte (SE) (argyrodite LPSCl). Lithiophilic 1 μm Li_2Te coating on standard planar copper current-collector significantly reduces electrodeposition/electrodissolution overpotentials and improves CE. During continuous plating experiments using half-cells (1 mA cm^{-2}), the accumulated thickness of electrodeposited Li on $\text{Li}_2\text{Te-Cu}$ is more than 70 μm , which is the thickness of the Li foil counter-electrode. The NMC811 anode-free cell (external pressure 13 MPa) delivers an initial CE of 83% at 0.2C, with a steady-state cycling CE above 99%. Cryo-FIB sectioning demonstrates uniform electrodeposited metal microstructure, with no signs of voids or dendrites at the collector-SE interface. Cryo-FIB also demonstrates that electrodisolution is uniform and complete, the lithiophilic coating remaining adherent on the collector. By contrast, a bare Cu collector promotes inhomogeneous Li electrodeposition/electrodissolution, electrochemically inactive “dead metal,” dendrites that extend into the SE, and extensive non-uniform SEI interspersed with pores. DFT and mesoscale calculations consider the thermodynamic stability of lithium atoms versus lithium clusters on Li_2Te and Cu surfaces, including subsurface effects after one monolayer is deposited as well as the nucleation-growth behavior. This work paves the way for viable AF-ASSBs that deliver significantly higher specific energies and cost less than ASSBs which require metal or ion-storing anodes.

4. Experimental Section

Materials Preparation: Te–Cu substrate: Commercial Cu foil (9 μm thickness, MTI, USA) was first cut into 2 $\text{cm} \times 5 \text{cm}$ pieces and cleaned with ethanol under sonication. To prepare Te–Cu, 2.5 mg Te powder was added to the bottom of a rectangular crucible with a piece of cleaned Cu foil placed on the top of it. The crucible was then transferred to a tube furnace and heated to 600 $^\circ\text{C}$ for 1 h at a ramping rate of 10 $^\circ\text{C min}^{-1}$ under a continuous Ar flow. After cooling down to room temperature, the Te–Cu was obtained and cut into disks with a diameter of 10 mm for electrochemical tests. The mass loading of Cu_2Te was $\approx 0.4 \text{ mg cm}^{-2}$. For comparison, Te–Cu with Cu_2Te mass loadings of 0.2 and 1 mg cm^{-2} were also prepared and denoted as $\text{Li}_2\text{Te-Cu-0.1}$ and $\text{Li}_2\text{Te-Cu-1}$.

$\text{Li}_6\text{PS}_5\text{Cl}$ solid-electrolyte: To prepare argyrodite electrolyte $\text{Li}_6\text{PS}_5\text{Cl}$, a stoichiometric amount of Li_2S (> 99.9%, Sigma Aldrich), P_2S_5 (>99.9%, Sigma Aldrich), and LiCl (> 99.9%, Sigma Aldrich) were ground together in an air-tight ZrO_2 jar with ZrO_2 balls using high energy ball-milling machine (SPEX SamplePrep, 8000M Mixer/Mill) for 2 h. The obtained powder was then sintered at 550 $^\circ\text{C}$ for 12 h in an Ar-filled glovebox. The

XRD profile is shown in Figure S21a, Supporting Information. The ionic conductivity at room temperature was measured to be 3.2 mS cm^{-1} , per Figure S21b, Supporting Information.

Battery Assembly: All-solid-state asymmetric half-cell: 150 mg solid electrolyte powder was first pressed under 75 MPa in a PEEK mold with a diameter of 12 mm. The surface layer of Li foils was removed with a blade and rolled to a thickness of around $100 \mu\text{m}$ before use. Then, a piece of Li foil and a Cu or Te–Cu foil were placed on two sides of the electrolyte pellets. The laminated battery was further pressed under 225 MPa to improve the contact between Li and electrolyte before being mounted to the cell holder with a stack pressure of $\approx 13 \text{ MPa}$.

Anode-free all-solid-state Li cell with $\text{LiNi}_{0.8}\text{Co}_{0.1}\text{Mn}_{0.1}\text{O}_2$ (NMC811) cathode: NMC811 (MSE corporation) was ground together with SE powder at a weight ratio of 8:2 without any carbon being added. When assembling the battery, 150 mg LPSCl powder was first pressed in PEEK mold under 75 MPa. Then about 5–10 mg cathode powder ($6\text{--}12 \text{ mg cm}^{-2}$) was uniformly dispersed on one side of the electrolyte and a piece of Cu or Te–Cu foil was placed on the other side. 225 MPa pressure was finally applied to the battery to get a close contact before electrochemical tests. Finally, the cells were mounted to the cell holder with a stack pressure of 13 MPa.

Electrochemical Measurements: The impedance tests of the half and full cells were conducted on a Princeton PARSTAT MC electrochemical workstation. A perturbation voltage of 10 mV in the frequency range of 1 MHz–0.1 Hz was applied. Z-view software was used to analyze the plot coupled with equivalent circuit fitting. The Li ionic conductivities of all the composite electrolytes were calculated based on the equation $\sigma = L/RS$, where L was the thickness of the pressed pellet, S was the area of the surface, and R was the resistance recorded using a PEEK cell. The galvanostatic charge/discharge profiles were recorded on a Land CT2001A system and all electrochemical tests were carried out at room temperature in this work.

Material Characterization: SEM images were collected using a field emission scanning electron microscope (Hitachi S-5500) equipped with an EDX. Cryo-EM analysis was performed on a Thermo Scientific Scios 2 Dual Beam SEM/FIB with a Leica VCT cryogenic stage and EDX detector. To preserve the structural integrity of the beam-sensitive Li-based materials and to reduce artificial inclusion, the sample was cooled to $-150 \text{ }^\circ\text{C}$. The Ga^+ FIB milling was performed at an accelerating voltage of 30 keV. XRD profiles were recorded on Rigaku Miniflex 600 diffractometer with Cu $K\alpha$ radiation ($\lambda = 1.54178 \text{ \AA}$) at a scan rate of 5° min^{-1} within the 2θ range from 10° to 80° . XPS analysis was performed on a customized XPS system based on a Hemispherical Energy Analyzer PHOIBOS 100 (SPECS Surface Nano Analysis GmbH) with Mg $K\alpha$ as the excitation source. All post-cycled electrodes were extracted from disassembled cells in an Ar-filled glovebox ($<0.1 \text{ ppm}$ of H_2O and O_2).

Computational Details: Structures were obtained from the Materials Project^[72] and were modified using VESTA.^[73] The DFT calculations were performed with the Vienna Ab initio Simulation Package.^[74] Electronic structures were optimized using the Perdew–Burke–Ernzerhof functional with the generalized gradient approximation. A cut-off energy of 400 eV and a gamma-centered k-point mesh of $4 \times 4 \times 4$ for bulk and $4 \times 4 \times 1$ for slab were used for the planewave basis with projector-augmented wave pseudopotential. For optimization, the convergence tolerances for the force and the energy were 0.01 eV \AA^{-1} and 10^{-6} eV , respectively.

Description of the mesoscale model: The mesoscale model captured the morphological evolution during electrodeposition of Li based on the kinetic Monte Carlo algorithm.^[112,123] The modeling framework and parameters have been described in this section. The Li–substrate interaction was described using $k_{\text{Li-substrate}}$ and $k_{\text{Li-Li}}$, which denoted the absorption rate of Li on the substrate and the absorption rate of Li on freshly deposited Li on the substrate, respectively. The effect of $k_{\text{Li-substrate}}$ and $k_{\text{Li-Li}}$ was captured in the model by mapping the kinetics of these events to the location of the substrate and spatial distribution of the deposited Li atoms. This process included the combination of lithium-ions with an electron required to form adsorbed lithium atoms

on the substrate and newly deposited lithium. The deposited metal atoms could diffuse across the deposition front based on their surface diffusion kinetics ($k_D = v \exp(-\frac{E_{a,D}}{k_B T})$). Based on these processes, a

total rate (k_{total}) was calculated, which was the sum of kinetic rates corresponding to the possible events of metal adsorption on the substrate and deposited metal morphology, metal diffusion across the deposition front and ion transport. Using k_{total} , the morphology evolution in the model was performed as follows: a random number r_1 was chosen between 0 and 1 and multiplied with k_{total} . All the possible processes in the system were scanned, and the first event for which the sum of rates of the previously scanned events was larger than $r_1 k_{\text{total}}$ was selected. The system was then evolved using the event that got selected based on this algorithm. In the kinetic Monte Carlo algorithm, the time step for each event was calculated using a random number

$$r_2: \delta t = -\frac{1}{k_{\text{tot}}} \ln r_2.$$

The parameters used in the mesoscale model have been presented in Table S1, Supporting Information.

Supporting Information

Supporting Information is available from the Wiley Online Library or from the author.

Acknowledgements

This work was supported by the Mechano-Chemical Understanding of Solid Ion Conductors, an Energy Frontier Research Center funded by the U.S. Department of Energy, Office of Science, Office of Basic Energy Science, contract DE-SC0023438. Microscopy analysis was performed at the Center for Integrated Nanotechnologies, an Office of Science User Facility operated for the U.S. Department of Energy (DOE) Office of Science. Los Alamos National Laboratory, an affirmative action equal opportunity employer, is managed by Triad National Security, LLC for the U.S. Department of Energy's NNSA, under contract 89233218CNA000001. Calculations performed by M.N., J.C., N.K., and G.H. were supported by the Welch Foundation (F-1841), and computing resources at the Extreme Science and Engineering Discovery Environment (XSEDE)/Advanced Cyberinfrastructure Coordination Ecosystem: Services and Support (ACCESS), and Texas Advanced Computing Center (TACC) with the allocation CHE190010 – Modeling Materials for Energy Conversion and Storage over Experimental Timescales.

Conflict of Interest

The authors declare no conflict of interest.

Data Availability Statement

The data that support the findings of this study are available from the corresponding author upon reasonable request.

Keywords

all-solid-state batteries, anode-free batteries, cryogenic microscopy, dead lithium, solid-state electrolytes

Received: July 25, 2022

Revised: October 23, 2022

Published online:

- [1] J. B. Goodenough, Y. Kim, *Chem. Mater.* **2009**, *22*, 587.
- [2] Y. Zhu, J. C. Gonzalez-Rosillo, M. Balaish, Z. D. Hood, K. J. Kim, J. L. M. Rupp, *Nat. Rev. Mater.* **2020**, *6*, 313.
- [3] D. H. S. Tan, A. Banerjee, Z. Chen, Y. S. Meng, *Nat. Nanotechnol.* **2020**, *15*, 170.
- [4] J. Janek, W. G. Zeier, *Nat. Energy* **2016**, *1*, 16141.
- [5] P. Albertus, V. Anandan, C. Ban, N. Balsara, I. Belharouak, J. Buettner-Garrett, Z. Chen, C. Daniel, M. Doeff, N. J. Dudney, B. Dunn, S. J. Harris, S. Herle, E. Herbert, S. Kalnaus, J. A. Libera, D. Lu, S. Martin, B. D. McCloskey, M. T. McDowell, Y. S. Meng, J. Nanda, J. Sakamoto, E. C. Self, S. Tepavcevic, E. Wachsman, C. Wang, A. S. Westover, J. Xiao, T. Yersak, *ACS Energy Lett.* **2021**, *6*, 1399.
- [6] M. Pasta, D. Armstrong, Z. L. Brown, J. Bu, M. R. Castell, P. Chen, C. Cocks, S. A. Corr, E. J. Cussen, E. Darnbrough, V. Deshpande, C. Doerr, M. S. Dyer, H. El-Shinawi, N. Fleck, P. Grant, G. L. Gregory, C. Grovenor, L. J. Hardwick, J. T. S. Irvine, H. J. Lee, G. Li, E. Liberti, I. McClelland, C. Monroe, P. D. Nellist, P. R. Shearing, E. Shoko, W. Song, D. S. Jolly, et al., *J. Phys.: Energy* **2020**, *2*, 032008.
- [7] S. Lou, F. Zhang, C. Fu, M. Chen, Y. Ma, G. Yin, J. Wang, *Adv. Mater.* **2021**, *33*, 2000721.
- [8] R. Wang, Q. Dong, C. Wang, M. Hong, J. Gao, H. Xie, M. Guo, W. Ping, X. Wang, S. He, J. Luo, L. Hu, *Adv. Mater.* **2021**, *33*, 2100726.
- [9] L. Li, S. Basu, Y. Wang, Z. Chen, P. Hundekar, B. Wang, J. Shi, Y. Shi, S. Narayanan, N. Koratkar, *Science* **2018**, *359*, 1513.
- [10] B. S. Vishnugopi, E. Kazayk, J. A. Lewis, J. Nanda, M. T. McDowell, N. P. Dasgupta, P. P. Mukherjee, *ACS Energy Lett.* **2021**, *6*, 3734.
- [11] L. Ye, X. Li, *Nature* **2021**, *593*, 218.
- [12] D. H. Tan, Y.-T. Chen, H. Yang, W. Bao, B. Sreenarayanan, J.-M. Doux, W. Li, B. Lu, S.-Y. Ham, B. Sayahpour, *Science* **2021**, *373*, 1494.
- [13] Y.-G. Lee, S. Fujiki, C. Jung, N. Suzuki, N. Yashiro, R. Omoda, D.-S. Ko, T. Shiratsuchi, T. Sugimoto, S. Ryu, J. H. Ku, T. Watanabe, Y. Park, Y. Aihara, D. Im, I. T. Han, *Nat. Energy* **2020**, *5*, 299.
- [14] Z. Cui, Q. Xie, A. Manthiram, *Adv. Energy Mater.* **2021**, *11*, 2102421.
- [15] O. Sheng, C. Jin, X. Ding, T. Liu, Y. Wan, Y. Liu, J. Nai, Y. Wang, C. Liu, X. Tao, *Adv. Funct. Mater.* **2021**, *31*, 2100891.
- [16] R. Fan, C. Liu, K. He, S. H.-S. Cheng, D. Chen, C. Liao, R. K. Y. Li, J. Tang, Z. Lu, *ACS Appl. Mater. Interfaces* **2020**, *12*, 7222.
- [17] Z. Zhang, Y. Shao, B. Lotsch, Y.-S. Hu, H. Li, J. Janek, L. F. Nazar, C.-W. Nan, J. Maier, M. Armand, L. Chen, *Energy Environ. Sci.* **2018**, *11*, 1945.
- [18] J. Liu, H. Yuan, H. Liu, C. Z. Zhao, Y. Lu, X. B. Cheng, J. Q. Huang, Q. Zhang, *Adv. Energy Mater.* **2021**, *12*, 2100748.
- [19] J. Han, H. Li, D. Kong, C. Zhang, Y. Tao, H. Li, Q.-H. Yang, L. Chen, *ACS Energy Lett.* **2020**, *5*, 1986.
- [20] C. Yu, F. Zhao, J. Luo, L. Zhang, X. Sun, *Nano Energy* **2021**, *83*, 105858.
- [21] D. Cao, X. Sun, Y. Li, A. Anderson, W. Lu, H. Zhu, *Adv. Mater.* **2022**, *34*, 2200401.
- [22] R. Kanno, M. Murayama, *J. Electrochem. Soc.* **2001**, *148*, A742.
- [23] A. Banerjee, X. Wang, C. Fang, E. A. Wu, Y. S. Meng, *Chem. Rev.* **2020**, *120*, 6878.
- [24] X. Li, J. Liang, J. T. Kim, J. Fu, H. Duan, N. Chen, R. Li, S. Zhao, J. Wang, H. Huang, X. Sun, *Adv. Mater.* **2022**, *34*, 2200856.
- [25] Y. Kato, S. Hori, T. Saito, K. Suzuki, M. Hirayama, A. Mitsui, M. Yonemura, H. Iba, R. Kanno, *Nat. Energy* **2016**, *1*, 16030.
- [26] N. Kamaya, K. Homma, Y. Yamakawa, M. Hirayama, R. Kanno, M. Yonemura, T. Kamiyama, Y. Kato, S. Hama, K. Kawamoto, A. Mitsui, *Nat. Mater.* **2011**, *10*, 682.
- [27] P. Adeli, J. D. Bazak, K. H. Park, I. Kochetkov, A. Huq, G. R. Goward, L. F. Nazar, *Angew. Chem., Int. Ed.* **2019**, *58*, 8681.
- [28] M. A. Kraft, S. P. Culver, M. Calderon, F. Bocher, T. Krauskopf, A. Senyshyn, C. Dietrich, A. Zevalkink, J. Janek, W. G. Zeier, *J. Am. Chem. Soc.* **2017**, *139*, 10909.
- [29] Z. Deng, Z. Wang, I.-H. Chu, J. Luo, S. P. Ong, *J. Electrochem. Soc.* **2015**, *163*, A67.
- [30] J. E. Lee, K. H. Park, J. C. Kim, T. U. Wi, A. R. Ha, Y. B. Song, D. Y. Oh, J. Woo, S. H. Kweon, S. J. Yeom, W. Cho, K. Kim, H. W. Lee, S. K. Kwak, Y. S. Jung, *Adv. Mater.* **2022**, *34*, 2200083.
- [31] J. Zhang, L. Li, C. Zheng, Y. Xia, Y. Gan, H. Huang, C. Liang, X. He, X. Tao, W. Zhang, *ACS Appl. Mater. Interfaces* **2020**, *12*, 41538.
- [32] Y. Seino, T. Ota, K. Takada, A. Hayashi, M. Tatsumisago, *Energy Environ. Sci.* **2014**, *7*, 627.
- [33] S. Randau, D. A. Weber, O. Kötz, R. Koerver, P. Braun, A. Weber, E. Ivers-Tiffée, T. Adermann, J. Kulisch, W. G. Zeier, F. H. Richter, J. Janek, *Nat. Energy* **2020**, *5*, 259.
- [34] K. Yoon, S. Lee, K. Oh, K. Kang, *Adv. Mater.* **2022**, *34*, 2104666.
- [35] C. Wang, S. Hwang, M. Jiang, J. Liang, Y. Sun, K. Adair, M. Zheng, S. Mukherjee, X. Li, R. Li, H. Huang, S. Zhao, L. Zhang, S. Lu, J. Wang, C. V. Singh, D. Su, X. Sun, *Adv. Energy Mater.* **2021**, *11*, 2100210.
- [36] Y. Zhao, K. Zheng, X. Sun, *Joule* **2018**, *2*, 2583.
- [37] J. Wu, S. Liu, F. Han, X. Yao, C. Wang, *Adv. Mater.* **2021**, *33*, 2000751.
- [38] Q. Tu, T. Shi, S. Chakravarthy, G. Ceder, *Matter* **2021**, *4*, 3248.
- [39] T. T. Zuo, R. Ruess, R. Pan, F. Walther, M. Rohnke, S. Hori, R. Kanno, D. Schroder, J. Janek, *Nat. Commun.* **2021**, *12*, 6669.
- [40] T. Brahmbhatt, G. Yang, E. Self, J. Nanda, *Front. Energy Res.* **2020**, *8*, 570754.
- [41] X. Y. Yue, Y. X. Yao, J. Zhang, Z. Li, S. Y. Yang, X. L. Li, C. Yan, Q. Zhang, *Angew. Chem., Int. Ed.* **2022**, *134*, 202205697.
- [42] P. Hartmann, T. Leichtweiss, M. R. Busche, M. Schneider, M. Reich, J. Sann, P. Adelhelm, J. Janek, *J. Phys. Chem. C* **2013**, *117*, 21064.
- [43] W. Guo, S. Liu, X. Guan, X. Zhang, X. Liu, J. Luo, *Adv. Energy Mater.* **2019**, *9*, 1900193.
- [44] P. Bron, B. Roling, S. Dehnen, *J. Power Sources* **2017**, *352*, 127.
- [45] T. Krauskopf, F. H. Richter, W. G. Zeier, J. Janek, *Chem. Rev.* **2020**, *120*, 7745.
- [46] B. Zahir, A. Patra, C. Kiggins, A. X. B. Yong, E. Ertekin, J. B. Cook, P. V. Braun, *Nat. Mater.* **2021**, *20*, 1392.
- [47] S. Wenzel, T. Leichtweiss, D. Krüger, J. Sann, J. Janek, *Solid State Ionics* **2015**, *278*, 98.
- [48] F. Han, Y. Zhu, X. He, Y. Mo, C. Wang, *Adv. Energy Mater.* **2016**, *6*, 1501590.
- [49] R. Koerver, I. Aygün, T. Leichtweiß, C. Dietrich, W. Zhang, J. O. Binder, P. Hartmann, W. G. Zeier, J. Janek, *Chem. Mater.* **2017**, *29*, 5574.
- [50] M. Suyama, S. Yubuchi, M. Deguchi, A. Sakuda, M. Tatsumisago, A. Hayashi, *J. Electrochem. Soc.* **2021**, *168*, 060542.
- [51] T. Hakari, M. Deguchi, K. Mitsuhara, T. Ohta, K. Saito, Y. Orikasa, Y. Uchimoto, Y. Kowada, A. Hayashi, M. Tatsumisago, *Chem. Mater.* **2017**, *29*, 4768.
- [52] T. K. Schwietert, V. A. Arszewska, C. Wang, C. Yu, A. Vasileiadis, N. J. J. de Klerk, J. Hageman, T. Hupfer, I. Kerkamm, Y. Xu, E. van der Maas, E. M. Kelder, S. Ganapathy, M. Wagemaker, *Nat. Mater.* **2020**, *19*, 428.
- [53] S. Wenzel, S. J. Sedlmaier, C. Dietrich, W. G. Zeier, J. Janek, *Solid State Ionics* **2018**, *318*, 102.
- [54] C. Zheng, J. Zhang, Y. Xia, H. Huang, Y. Gan, C. Liang, X. He, X. Tao, W. Zhang, *Small* **2021**, *17*, 2101326.
- [55] D. Cao, X. Sun, Q. Li, A. Natan, P. Xiang, H. Zhu, *Matter* **2020**, *3*, 57.
- [56] X. Feng, H. Fang, N. Wu, P. Liu, P. Jena, J. Nanda, D. Mitlin, *Joule* **2022**, *6*, 543.
- [57] Y. Liu, C. Li, B. Li, H. Song, Z. Cheng, M. Chen, P. He, H. Zhou, *Adv. Energy Mater.* **2018**, *8*, 1702374.

- [58] S. Wang, J. Wang, J. Liu, H. Song, Y. Liu, P. Wang, P. He, J. Xu, H. Zhou, *J. Mater. Chem. A* **2018**, *6*, 21248.
- [59] O. Sheng, C. Jin, M. Chen, Z. Ju, Y. Liu, Y. Wang, J. Nai, T. Liu, W. Zhang, X. Tao, *J. Mater. Chem. A* **2020**, *8*, 13541.
- [60] O. Sheng, H. Hu, T. Liu, Z. Ju, G. Lu, Y. Liu, J. Nai, Y. Wang, W. Zhang, X. Tao, *Adv. Funct. Mater.* **2021**, *32*, 2111026.
- [61] S. E. Sandoval, F. J. Q. Cortes, E. J. Klein, J. A. Lewis, P. P. Shetty, D. Yeh, M. T. McDowell, *J. Electrochem. Soc.* **2021**, *168*, 100517.
- [62] S. Y. Han, C. Lee, J. A. Lewis, D. Yeh, Y. Liu, H.-W. Lee, M. T. McDowell, *Joule* **2021**, *5*, 2450.
- [63] H. Zhong, L. Sang, F. Ding, J. Song, Y. Mai, *Electrochim. Acta* **2018**, *277*, 268.
- [64] R. B. Cervera, N. Suzuki, T. Ohnishi, M. Osada, K. Mitsuishi, T. Kambara, K. Takada, *Energy Environ. Sci.* **2014**, *7*, 662.
- [65] J. Wan, Y. X. Song, W. P. Chen, H. J. Guo, Y. Shi, Y. J. Guo, J. L. Shi, Y. G. Guo, F. F. Jia, F. Y. Wang, R. Wen, L. J. Wan, *J. Am. Chem. Soc.* **2021**, *143*, 839.
- [66] R. Xu, J. F. Ding, X. X. Ma, C. Yan, Y. X. Yao, J. Q. Huang, *Adv. Mater.* **2021**, *33*, 2105962.
- [67] J. Kasemchainan, S. Zekoll, D. S. Jolly, Z. Ning, G. O. Hartley, J. Marrow, P. G. Bruce, *Nat. Mater.* **2019**, *18*, 1105.
- [68] T. Krauskopf, H. Hartmann, W. G. Zeier, J. Janek, *ACS Appl. Mater. Interfaces* **2019**, *11*, 14463.
- [69] R. Weber, M. Genovese, A. J. Louli, S. Hames, C. Martin, I. G. Hill, J. R. Dahn, *Nat. Energy* **2019**, *4*, 683.
- [70] A. J. Louli, A. Eldesoky, R. Weber, M. Genovese, M. Coon, J. deGooyer, Z. Deng, R. T. White, J. Lee, T. Rodgers, R. Petibon, S. Hy, S. J. H. Cheng, J. R. Dahn, *Nat. Energy* **2020**, *5*, 693.
- [71] M. Genovese, A. J. Louli, R. Weber, S. Hames, J. R. Dahn, *J. Electrochem. Soc.* **2018**, *165*, A3321.
- [72] S. Chen, J. Zhang, L. Nie, X. Hu, Y. Huang, Y. Yu, W. Liu, *Adv. Mater.* **2021**, *33*, 2002325.
- [73] C. Heubner, S. Maletti, H. Auer, J. Hüttel, K. Voigt, O. Lohrberg, K. Nikolowski, M. Partsch, A. Michaelis, *Adv. Funct. Mater.* **2021**, *31*, 2106608.
- [74] J. Qian, B. D. Adams, J. Zheng, W. Xu, W. A. Henderson, J. Wang, M. E. Bowden, S. Xu, J. Hu, J.-G. Zhang, *Adv. Funct. Mater.* **2016**, *26*, 7094.
- [75] B. Neudecker, N. Dudney, J. Bates, *J. Electrochem. Soc.* **2000**, *147*, 517.
- [76] A. S. Westover, R. L. Sacci, N. Dudney, *ACS Energy Lett.* **2020**, *5*, 3860.
- [77] D. Cheng, R. Shimizu, J. Weaver, Y. S. Meng, *Microsc. Microanal.* **2021**, *27*, 3324.
- [78] M. J. Wang, E. Carmona, A. Gupta, P. Albertus, J. Sakamoto, *Nat. Commun.* **2020**, *11*, 5201.
- [79] H. Hao, T. Hutter, B. L. Boyce, J. Watt, P. Liu, D. Mitlin, *Chem. Rev.* **2022**, *122*, 8053.
- [80] W. D. Richards, L. J. Miara, Y. Wang, J. C. Kim, G. Ceder, *Chem. Mater.* **2015**, *28*, 266.
- [81] X. Li, D. Wang, H. Wang, H. Yan, Z. Gong, Y. Yang, *ACS Appl. Mater. Interfaces* **2019**, *11*, 22745.
- [82] K. Fu, Y. Gong, B. Liu, Y. Zhu, S. Xu, Y. Yao, W. Luo, C. Wang, S. D. Lacey, J. Dai, *Sci. Adv.* **2017**, *3*, e1601659.
- [83] L. Lin, L. Suo, Y. s. Hu, H. Li, X. Huang, L. Chen, *Adv. Energy Mater.* **2021**, *11*, 2003709.
- [84] A. A. Assegie, C. C. Chung, M. C. Tsai, W. N. Su, C. W. Chen, B. J. Hwang, *Nanoscale* **2019**, *11*, 2710.
- [85] B. Lee, E. Paek, D. Mitlin, S. W. Lee, *Chem. Rev.* **2019**, *119*, 5416.
- [86] W. Liu, P. Liu, D. Mitlin, *Chem. Soc. Rev.* **2020**, *49*, 7284.
- [87] W. Liu, P. Liu, D. Mitlin, *Adv. Energy Mater.* **2020**, *10*, 2002297.
- [88] P. Liu, Y. Wang, Q. Gu, J. Nanda, J. Watt, D. Mitlin, *Adv. Mater.* **2020**, *32*, 1906735.
- [89] K. Yan, Z. Lu, H.-W. Lee, F. Xiong, P.-C. Hsu, Y. Li, J. Zhao, S. Chu, Y. Cui, *Nat. Energy* **2016**, *1*, 16010.
- [90] A. Pei, G. Zheng, F. Shi, Y. Li, Y. Cui, *Nano Lett.* **2017**, *17*, 1132.
- [91] B. Thirumalraj, T. T. Hagos, C. J. Huang, M. A. Teshager, J. H. Cheng, W. N. Su, B. J. Hwang, *J. Am. Chem. Soc.* **2019**, *141*, 18612.
- [92] X. Chen, X.-R. Chen, T.-Z. Hou, B.-Q. Li, X.-B. Cheng, R. Zhang, Q. Zhang, *Sci. Adv.* **2019**, *5*, eaau7728.
- [93] M. J. Wang, E. Kazyak, N. P. Dasgupta, J. Sakamoto, *Joule* **2021**, *5*, 1371.
- [94] W. Chang, R. May, M. Wang, G. Thorsteinsson, J. Sakamoto, L. Marbella, D. Steingart, *Nat. Commun.* **2021**, *12*, 6369.
- [95] M. B. Dixit, B. S. Vishugopi, W. Zaman, P. Kenesei, J. S. Park, J. Almer, P. P. Mukherjee, K. B. Hatzell, *Nat. Mater.* **2022**, *21*, 1298.
- [96] V. Raj, V. Venturi, V. R. Kankanallu, B. Kuri, V. Viswanathan, N. P. B. Aetukuri, *Nat. Mater.* **2022**, *21*, 1050.
- [97] C. Kim, J. Kim, J. Park, J. Kim, S. Lee, S. Sun, S. Myung, D. Lee, K. Park, I. Jang, S. Kim, H. Lee, H. Jung, U. Paik, T. Song, *Adv. Energy Mater.* **2021**, *11*, 2102045.
- [98] C. Han, Z. Li, W.-j. Li, S.-I. Chou, S.-x. Dou, *J. Mater. Chem. A* **2014**, *2*, 11683.
- [99] C.-M. Park, Y.-U. Kim, H. Kim, H.-J. Sohn, *J. Power Sources* **2006**, *158*, 1451.
- [100] Z. Shi, M. Liu, D. Naik, J. L. Gole, *J. Power Sources* **2001**, *92*, 70.
- [101] Y. Hamon, T. Brousse, F. Jousse, P. Topart, P. Buvat, D. Schleich, *J. Power Sources* **2001**, *97*, 185.
- [102] D. M. Piper, T. A. Yersak, S.-H. Lee, *J. Electrochem. Soc.* **2012**, *160*, A77.
- [103] A. L. Santhosha, L. Medenbach, J. R. Buchheim, P. Adelhelm, *Batter Supercaps* **2019**, *2*, 524.
- [104] C. Arbizzani, S. Beninati, M. Lazzari, M. Mastragostino, *J. Power Sources* **2006**, *158*, 635.
- [105] J. U. Seo, G. K. Seong, C. M. Park, *Sci. Rep.* **2015**, *5*, 7969.
- [106] Y. Wang, H. Dong, N. Katyal, H. Hao, P. Liu, H. Celio, G. Henkelman, J. Watt, D. Mitlin, *Adv. Mater.* **2022**, *34*, 2106005.
- [107] J. Xu, J. Li, Y. Li, M. Yang, L. Chen, H. Li, F. Wu, *Adv. Mater.* **2022**, *34*, 2203281.
- [108] B. D. Adams, J. Zheng, X. Ren, W. Xu, J. G. Zhang, *Adv. Energy Mater.* **2017**, *8*, 1702097.
- [109] F. Qiu, X. Li, H. Deng, D. Wang, X. Mu, P. He, H. Zhou, *Adv. Energy Mater.* **2018**, *9*, 1803372.
- [110] J. M. Doux, H. Nguyen, D. H. S. Tan, A. Banerjee, X. Wang, E. A. Wu, C. Jo, H. Yang, Y. S. Meng, *Adv. Energy Mater.* **2019**, *10*, 1903253.
- [111] D. H. S. Tan, E. A. Wu, H. Nguyen, Z. Chen, M. A. T. Marple, J.-M. Doux, X. Wang, H. Yang, A. Banerjee, Y. S. Meng, *ACS Energy Lett.* **2019**, *4*, 2418.
- [112] B. S. Vishnugopi, F. Hao, A. Verma, P. P. Mukherjee, *Phys. Chem. Chem. Phys.* **2020**, *22*, 11286.
- [113] B. S. Vishnugopi, F. Hao, A. Verma, P. P. Mukherjee, *ACS Appl. Mater. Interfaces* **2020**, *12*, 23931.
- [114] B. S. Vishnugopi, M. B. Dixit, F. Hao, B. Shyam, J. B. Cook, K. B. Hatzell, P. P. Mukherjee, *Adv. Energy Mater.* **2021**, *12*, 2102825.
- [115] J. Auvergniot, A. Cassel, J.-B. Ledeuil, V. Viallet, V. Seznec, R. Dedyèvre, *Chem. Mater.* **2017**, *29*, 3883.
- [116] R. Koerver, W. Zhang, L. de Biasi, S. Schweißler, A. O. Kondrakov, S. Kolling, T. Brezesinski, P. Hartmann, W. G. Zeier, J. Janek, *Energy Environ. Sci.* **2018**, *11*, 2142.
- [117] H.-H. Ryu, K.-J. Park, C. S. Yoon, Y.-K. Sun, *Chem. Mater.* **2018**, *30*, 1155.
- [118] X. Liu, J. Shi, B. Zheng, Z. Chen, Y. Su, M. Zhang, C. Xie, M. Su, Y. Yang, *ACS Appl. Mater. Interfaces* **2021**, *13*, 41669.
- [119] A. Banerjee, H. Tang, X. Wang, J. H. Cheng, H. Nguyen, M. Zhang, D. H. S. Tan, T. A. Wynn, E. A. Wu, J. M. Doux, T. Wu, L. Ma, G. E. Sterbinsky, M. S. D'Souza, S. P. Ong, Y. S. Meng, *ACS Appl. Mater. Interfaces* **2019**, *11*, 43138.

- [120] C. Doerrer, I. Capone, S. Narayanan, J. Liu, C. R. M. Grovenor, M. Pasta, P. S. Grant, *ACS Appl. Mater. Interfaces* **2021**, *13*, 37809.
- [121] F. Strauss, J. H. Teo, J. Maibach, A. Y. Kim, A. Mazilkin, J. Janek, T. Brezesinski, *ACS Appl. Mater. Interfaces* **2020**, *12*, 57146.
- [122] G. V. Alexander, N. C. Rosero-Navarro, A. Miura, K. Tadanaga, R. Murugan, *J. Mater. Chem. A* **2018**, *6*, 21018.
- [123] A. F. Voter, in *Radiation Effects in Solids*, Springer, Berlin **2007**, pp. 1–23.